

Coupled dynamics of the co-evolution of gravel bed topography, flow turbulence and sediment transport in an experimental channel

Arvind Singh,^{1,2} Efi Foufoula-Georgiou,^{1,2} Fernando Porté-Agel,^{1,3} and Peter R. Wilcock^{2,4}

Received 30 December 2011; revised 28 August 2012; accepted 30 August 2012; published 27 October 2012.

[1] A series of flume experiments were conducted in a large experimental channel at the St. Anthony Falls Laboratory to understand the coupled dynamics of flow and bed forms above the sediment-water interface. Simultaneous high resolution measurements of velocity fluctuations, bed elevations and sediment flux at the downstream end of the channel, were made for a range of discharges. The probability density functions (pdfs) of bed elevation increments and instantaneous Reynolds stress reveal a power law tail behavior and a wavelet cross-correlation analysis depicts a strong dependence of these series across a range of scales, indicating a feedback between bed form dynamics and near-bed turbulence. These results complement our previous findings in which the signature of bed form evolution on the near-bed velocity fluctuations was confirmed via the presence of a spectral gap and two distinct power law scaling regimes in the spectral density of velocity fluctuations. We report herein a strong asymmetry in the probability distribution of bed elevation increments and instantaneous Reynolds stresses, the latter being further analyzed and interpreted via a quadrant analysis of velocity fluctuations in the longitudinal and vertical directions. We also report the presence of intermittency (multifractality) in bed elevation increments and interpret it, in view of the asymmetric nature of the pdfs, as the result of scale coupling. In other words, the geometric asymmetry at the bed form scale gets transferred down to a probabilistic asymmetry at all smaller scales indicating a local anisotropy in the energy transfer. Finally, we propose a predictive relationship between bed form averaged sediment transport rates and bed form averaged instantaneous Reynolds stress and validate it using our experimental data.

Citation: Singh, A., E. Foufoula-Georgiou, F. Porté-Agel, and P. R. Wilcock (2012), Coupled dynamics of the co-evolution of gravel bed topography, flow turbulence and sediment transport in an experimental channel, *J. Geophys. Res.*, 117, F04016, doi:10.1029/2011JF002323.

1. Introduction

[2] One of the most striking features of turbulence is the stochastic nature of its eddies and their self-similar behavior over a range of scales [Kolmogorov, 1941; Batchelor and Townsend, 1949; Castaing *et al.*, 1990; Malecot *et al.*, 2000]. The energy cascades from large scale flow structures (large eddies) to the small scale flow structures by an inertial and inviscid mechanism. As documented earlier by

many researchers, these turbulent eddies play an important role in river morphodynamics, as well as sediment and nutrient transport [Nikora and Goring, 2000; Shvidchenko and Pender, 2001; Maddux *et al.*, 2003; Nelson *et al.*, 2006; Best, 2005; Hardy *et al.*, 2009, 2010]. They interact with the fluvial bed over a wide range of scales, from the scale of the grain, to the scale of the bed forms [Nikora, 2008; Singh *et al.*, 2010]. Depending on the size and position of these eddies, they can exert shear on the boundary (bed surface, banks, etc.), which, in turn, mobilizes the material present on it (the higher the boundary shear stress, the larger the rate of sediment transport). Due to the spatial and temporal variability in sediment transport rates (caused by variability in local shear stress), bed forms are dynamically created and modified, and in turn, their presence induces flow acceleration/deceleration further modulating sediment transport. Hence, a strong feedback exists between flow turbulence, bed topography and sediment transport.

[3] The evolution and spatial characteristics of bed forms are also strongly affected by the substrate composition, i.e., the bed material grain size distribution [e.g., Kleinhans *et al.*,

¹Department of Civil Engineering, St. Anthony Falls Laboratory, University of Minnesota, Twin Cities, Minneapolis, Minnesota, USA.

²National Center for Earth-Surface Dynamics, Minneapolis, Minnesota, USA.

³Wind Engineering and Renewable Energy Laboratory, ENAC-IIE-WIRE, École Polytechnique Fédérale de Lausanne, Lausanne, Switzerland.

⁴Department of Geography and Environmental Engineering, Johns Hopkins University, Baltimore, Maryland, USA.

Corresponding author: E. Foufoula-Georgiou, Department of Civil Engineering, St. Anthony Falls Laboratory, University of Minnesota, Twin Cities, Minneapolis, MN 55414, USA. (efi@umn.edu)

2002]. For example, in a gravel bed channel, a wider grain size distribution may produce more variable bed forms particularly when grains of different size tend to sort and produce bed forms of different size. On the other hand, two fluvial beds with similar grain size distribution, subjected to different discharge rates, will produce larger and more variable bed forms (and, in general, more variable bed topography at all scales) at higher discharge as compared to lower discharge. As a result of a wide range of scales of bed forms produced by the combination of grain size and flow conditions, the turbulence field will be different, perhaps more variable in the presence of many scales and sizes of bed forms. In a recent work [Singh et al., 2010] have shown that with increasing discharge, the slope of the power spectral density of temporal bed elevation increases. Moreover, in that particular study they have shown that the migrating bed topography imprints a distinct signature on the near-bed velocity fluctuations. This has also been conceptually shown in [Nikora, 2008].

[4] The effect of bed topography on flow structures and sediment transport has been quantified by several studies both in sand-bed [e.g., McLean and Smith, 1979; Best, 1993, 2005; Jerolmack and Mohrig, 2005; Venditti, 2007] and gravel bed channels [e.g., Shvidchenko and Pender, 2001; Nikora et al., 1998; Nikora and Walsh, 2004; Lamarre and Roy, 2005]. However, most of these studies were conducted either on a flat bed or on an immobile bed. To the best of our knowledge there are very few studies which quantify the interaction of bed topography with flow turbulence over migrating bed forms in a gravel bed environment [Dinehart, 1992, 1999; Shvidchenko and Pender, 2001; Roy et al., 2004; Singh et al., 2010].

[5] The purpose of this study is to understand and quantify the co-evolution of bed topography and turbulent velocity fluctuations for a range of discharges and the signature of this co-evolution on the variability of the bedload transport rates. Based on our previous studies of [Singh et al., 2009a] where the multiscale variability of sediment transport rates was characterized and [Singh et al., 2010] where the signature of migrating bed topography on the power spectral density of velocity fluctuations was quantified, we present here the results of a comprehensive analysis of simultaneous space-time characterization of gravel bed elevation, near-bed 3D turbulence, and sediment transport fluctuations, using data obtained in a large-scale laboratory experimental flume for a range of discharges. The paper is structured as follows. In section 2, a brief review of the experimental setup and the data collected is given. Section 3 is devoted to the characterization and quantification of the marginal statistics of bed elevations, instantaneous Reynolds stress, and sediment transport. Higher-order multiscale statistics of bed elevations are presented in section 4 followed, in section 5, by a physical interpretation of the asymmetry in the instantaneous Reynolds stress using a quadrant analysis. Section 6 quantifies the scale-to-scale interaction of bed elevations and instantaneous Reynolds stress using wavelet analysis. Section 7 focusses on predictive modeling of bedload transport as a function of instantaneous Reynolds stress. Finally, a hypothesis for interpreting intermittency (multi-fractality) in bed elevation increments in view of the

asymmetry in their pdfs is presented in section 8 followed by concluding remarks as section 9.

2. Experimental Setup and Data Analyzed

2.1. Experimental Setup

[6] Experiments were conducted in the Main Channel facility at the St. Anthony Falls Laboratory, University of Minnesota, as part of Streamlab08, a follow-up of the interdisciplinary project StreamLab06 (see some discussion in Wilcock et al. [2008] and Singh et al. [2010]). The scope of the StreamLab06 and StreamLab08 experiments, with details about the various studies conducted, data collected and the information about the data archived, can be found in A. Singh et al. (StreamLab: Overview of experiments, instrumentation, and data collected, submitted to *Water Resources Research*, 2012). The Main channel is 84 m long, 2.75 m wide and has a maximum depth of 1.8 m with a maximum discharge capacity 8000 l/s. It is a sediment recirculating channel while the water flows through the channel without recirculation. Intake of the water in the channel was directly from the Mississippi river. This experiment utilized only the upstream 55 m long section of the channel.

[7] The channel bed was composed of a mixture of gravel (median particle size diameter, $d_{50} = 11.3$ mm) and sand (median particle size diameter, $d_{50} = 1$ mm), with an overall grain size distribution with $d_{50} = 7.7$ mm, $d_{16} = 2.2$ mm and $d_{84} = 21.2$ mm. The mean specific density of sediment of all size fractions was ~ 2.65 . The thickness of the bed at the start of the run was approximately 0.45 m. Continuous data collection occurred for about twenty hours after the channel had reached quasi-dynamic equilibrium. This dynamic equilibrium state was evaluated by checking the stability of the 60 min average total sediment flux at the downstream end of the channel. Dynamic equilibrium was assumed to be reached when variation in this value became negligible. In other words, when the average of the previous 60 min of instantaneous sediment flux values computed from the pan data stabilized, we determined the channel to be in dynamic equilibrium and proceeded with formal data collection and sampling. More details about the experimental setup can be found in [Singh et al., 2009a, 2009b, 2010].

[8] The data collected included velocity and bed elevation at several locations as well as sediment flux at the downstream end of the channel (see Figure 1). The velocity fluctuations were measured at a frequency of 200 Hz using Acoustic Doppler Velocimeter (ADV) at an approximate distance of 10 cm above the mean bed level and 20 cm upstream of sonar 3. Table 1 shows the other relevant flow parameters and the distance of ADV from the mean bed elevation (D_p) for other discharges. Although the distance D_p changes with increasing discharge, the ratio k (where $k = D_p/\sigma_b$, σ_b = std. dev. of bed elevation) remains constant and ~ 5 . Bed elevations were sampled using submersible sonar transducers of 2.5 cm diameter which were deployed 0.3 m (on an average) below the water surface. The sampling interval of bed elevation measurements was 5 s with a vertical precision of 1 mm. For sampling sediment transport rates, bedload traps located at the downstream end of the test section, consisting of 5 weighing pans of equal size that

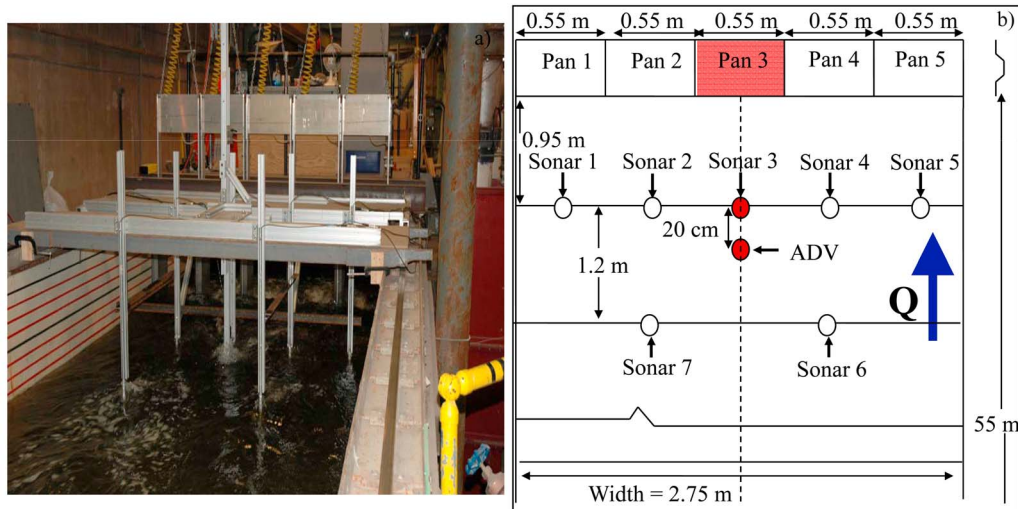


Figure 1. (a) Experimental channel facility at the St. Anthony Falls Laboratory, University of Minnesota and, (b) schematic diagram showing the location of probes in the experimental channel. Sediment flux data were collected at five downstream pans, bed elevations at seven sonar locations and the velocity fluctuations at one ADV location, for three different discharges. Note that the shaded parts (solid dots and box) along the centerline (dashed line) as we move from upstream to downstream represent the locations of velocity ($v(t)$), temporal bed elevation ($h(t)$) and sediment transport rates ($S(t)$), respectively, used in this study.

spanned the width of the channel, were used. Any bedload sediment transported to the end of the test-section of the channel would fall into the weigh pans, which automatically recorded the mass they contained every 1.1 s. Upon filling with a maximum of 40 kg, the weigh pans would tip to release the sediment and reset the weigh pan. The released sediment was re-circulated and released back into the channel at the upstream end of the 55 m test section, to maintain a closed system.

[9] Sediment transport rates sampled at a resolution of 1.1 s showed some negative values [see also Singh *et al.*, 2009a], which are not physically possible. To remove this noise some averaging was performed. Specifically, a moving average window (back-averaged) of 5 min was used, although it was found that the negative values were eliminated by a moving average window of only 2 min in size.

[10] Figures 1a (photo) and 1b (schematic) show the setup of the ADV, the sonars and sediment monitoring weigh pan system placed at the downstream end of the channel. Measurements were taken over a range of discharges corresponding to different bed shear stresses. For steady and uniform flow, bed shear stress is often characterized in terms of the dimensionless Shields stress, τ_b^* , and can be approximated as

$$\tau_b^* = \frac{h_R S}{(R - 1)d_{50}}, \quad (1)$$

where h_R and S are the hydraulic radius and channel slope, respectively, and $R = 2.65$ is the specific density of the sediment.

Table 1. Hydraulic Conditions and Statistics of Temporal Bed Elevation and Bed Forms

Q^a (l/s)	D^b (m)	V^c (m/s)	S_w^d (m)	h_R^e (m)	Shields Stress (τ_b^*) ^f	$Re = VD/\nu^g$	T_{mean}^h (°C)	D_p^i (cm)	σ_b^j (cm)	k^k	$\overline{\langle h_{bf} \rangle}^l$ (cm)	$std(h_{bf})^m$ (cm)
1500	0.43	1.27	0.0019	0.33	0.049	545455	17.9	9.26	1.58	5.8	3.38	0.98
2000	0.55	1.32	0.0019	0.39	0.058	727273	23.5	12.59	2.45	5.2	4.77	1.83
2800	0.64	1.59	0.0029	0.44	0.099	1018182	16.23	19.17	3.86	5.0	8.23	2.79

^aWater discharge for the run.

^bAverage depth of flow in test section.

^cAverage flow velocity.

^dWater surface slope.

^eHydraulic radius.

^fDimensionless Shields stress (computed using hydraulic radius).

^gReynolds number (kinematic viscosity of water, $\nu = 1 \times 10^{-6}$ m²/s).

^hMean water temperature.

ⁱDistance of the velocity probe from mean bed level.

^jStandard deviation of bed elevation.

^kRatio between D_p and σ_b .

^lMean bedform height obtained from the ensemble of bedform heights extracted from different probe locations.

^mStandard deviation of bedform heights obtained from the ensemble of bedform heights extracted from different probe locations. See section 3.1 for details.

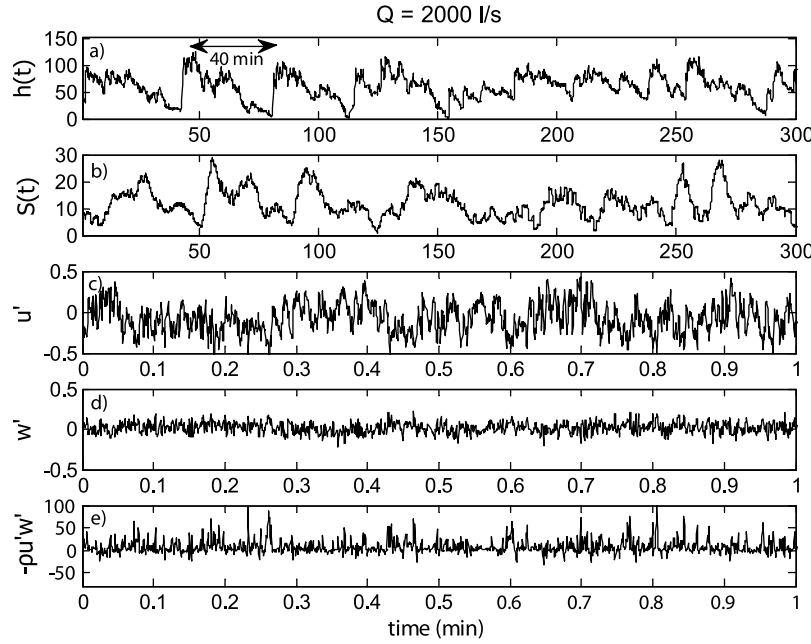


Figure 2. Time series of: (a) bed elevation (mm), (b) sediment transport rates ($\text{kg}/\text{m}/\text{min}$), (c) velocity fluctuations in the longitudinal direction (m/s), (d) velocity fluctuations in vertical direction (m/s) and, (e) instantaneous Reynolds stress ($\text{kg}/\text{m}/\text{s}^2$). The flow direction in the case of bed elevation (Figure 2a) is from the right to the left of the figure. Note that $h(t) = 0$ corresponds to the lowest observed elevation in the bed topography (not necessarily the base of the flume). The $S(t)$ series is obtained by using an averaging window of 5 min. For brevity we have shown the measurements for only 2000 l/s.

[11] Here we report the data collected at discharges of 1500 l/s, 2000 l/s and 2800 l/s. The aspect ratio (ratio of flume width to flow depth) for these experiments were 6.4, 5 and 4.3 for the discharges of 1500 l/s, 2000 l/s and 2800 l/s, respectively. As the data were collected in the fall season, there were some leaves floating in the channel which might have resulted in spikes in the velocity and bed elevation data. Even though the amount of spurious spikes in the data was found to be very small, these were removed as part of the data quality control [Singh et al., 2010; Parsheh et al., 2010].

2.2. Data Analyzed

[12] Figure 2 shows the data collected for the discharge of 2000 l/s. The bed elevations ($h(t)$) sampled using sonar 3 are shown in Figure 2a, simultaneously sampled 5 min averaged (moving average) sediment transport series ($S(t)$) in Figure 2b, velocity fluctuations around the mean in the flow direction (u') as Figure 2c, velocity fluctuations around the mean in the vertical direction (w') as Figure 2d, and the instantaneous Reynolds stress computed as the product of u' and w' ($\tau(t) = -\rho u' w'$, where ρ is the density of the water assumed to $1000 \text{ kg}/\text{m}^3$) is shown in Figure 2e. Note that we will use the terminology ‘instantaneous Reynolds stress’ for the product of $\rho u' w'$ and it is not to be confused with ‘local Reynolds stress’ or ‘Reynolds stress’ which is the average of instantaneous Reynolds stress ($\overline{-\rho u' w'}$). The increments of a signal $X(t)$ are denoted as $\Delta X(t)$ (obtained by differencing the signal, i.e., $\Delta X(t) = X(t+1) - X(t)$) whereas $X'(t)$ denotes the ‘fluctuations around the mean’ i.e., the mean

removed signal. The flow direction in the case of bed topography (Figure 2a) is from right to left of the figure. Note that in some cases, for brevity, we have shown the results for the discharge of 2000 l/s only since it represents the intermediate discharge, however, similar analysis were performed on the data at other discharges.

3. Marginal Statistics (Pdfs) of $\Delta h(t)$, $\tau(t)$ and $\Delta S(t)$

3.1. Physical Characteristics of Bed Topography

[13] Bed forms were formed on the gravel bed surface of the Main channel. They were mainly bedload sheets at the low discharge and transitioned to dunes as the discharge increased. Table 1 shows the statistics of the bed form heights for the discharges of 1500 l/s, 2000 l/s and 2800 l/s. The average bed form heights extracted from the temporal bed elevations using the methodology described in Singh et al. [2011] for the discharges of 1500 l/s, 2000 l/s and 2800 l/s were 3.38 cm, 4.77 cm and 8.23 cm while their standard deviations were 0.98 cm, 1.83 cm and 2.79 cm, respectively. Notice that with increasing discharge both the mean and the standard deviation of the bed form heights increases. Figure 3a shows the cumulative frequency histograms of the standardized bed form heights ($(h_{bf} - \langle h_{bf} \rangle)/\text{std}(h_{bf})$) for the discharges of 1500 l/s, 2000 l/s and 2800 l/s, where h_{bf} denotes the bed form height, $\text{std}(\cdot)$ the standard deviation of bed form heights, $\langle \cdot \rangle$ the average of bed form heights extracted from one probe, and $\overline{\langle \cdot \rangle}$ the ensemble average of bed form heights extracted from different probe

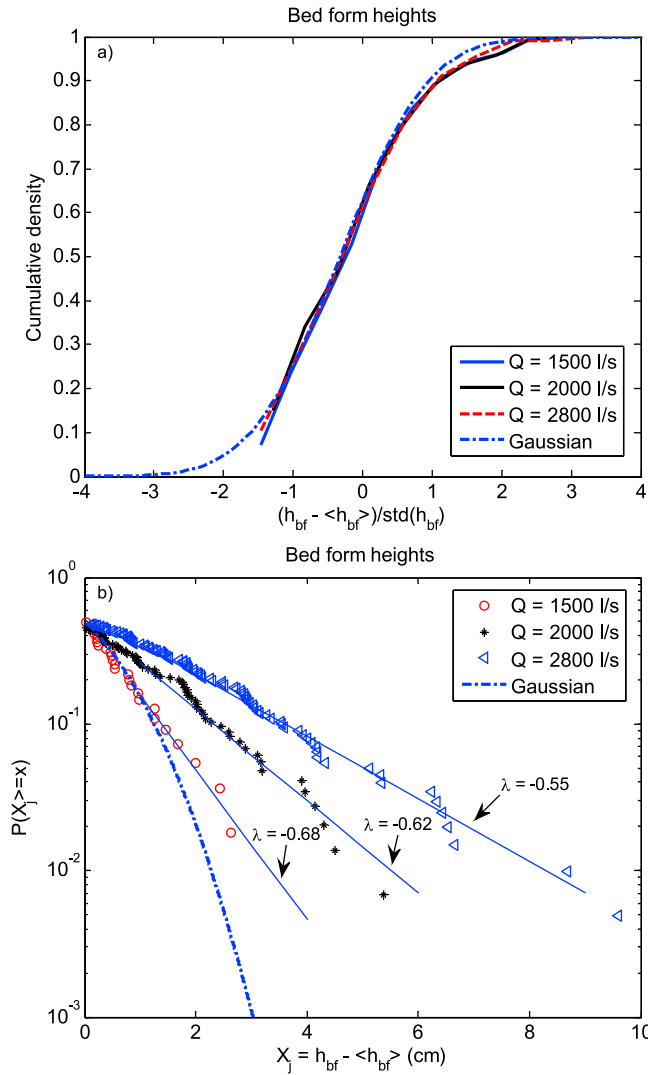


Figure 3. (a) Cumulative density function of normalized bed form heights (h_{bf}) obtained from the time series of bed elevation for the discharges of 1500 l/s, 2000 l/s and 2800 l/s. (b) Probability of exceedance of the positive part of the pdf of mean-removed bed form heights. Note that the broken line depicts the Gaussian distribution (computed using the std. dev. of the lowest discharge, 1500 l/s, which is ~ 1) whereas the solid lines in Figure 3b represent the exponential fit to the data. Also, note that the distribution of bed form heights for each discharge was obtained from the ensemble of bed forms heights extracted from the probes 2, 3, 4, 6 and 7 at that particular discharge.

locations. Note that the number of bed form heights h_{bf} extracted from the bed elevation series $h(t)$, varies from probe to probe as a result of lateral heterogeneities in the bed. The distributions of bed form heights for each discharge were obtained from the ensemble of bed form heights extracted from the temporal bed elevations collected at probes 2, 3, 4, 6 and 7 (see Figure 1b) for that particular discharge, respectively. From the normalized cumulative distribution plots of Figure 3a, it is observed that the distribution of bed form

heights does not change its shape significantly as a function of discharge and that the positive tails seem to deviate only slightly from those of the Gaussian distribution (also shown for comparison in Figure 3a). Note that, in the previous literature, the bed form heights have been reported to follow Gaussian, Gamma and Weibull distributions [see, e.g., *Paola and Borgman, 1991; van der Mark et al., 2008*]. To further explore the tail-behavior of the bed form heights, the probability of exceedance of the positive mean-removed bed form heights was computed as a function of discharge (Figure 3b). These exceedance plots suggest an exponential type of decay whose rate parameter λ decreases with increasing discharge.

[14] In addition to the extracted bed form heights, the “bed form average timescale”, i.e., the average time between two consecutive bed form crests, was computed for each discharge and was found to be 26.28 min, 22.02 min and 14.73 min, respectively, for discharges of 1500 l/s, 2000 l/s, and 2800 l/s, suggesting, as expected, that at higher discharges bed forms were moving faster.

3.2. Asymmetry Analysis of the Pdfs

[15] In this section we analyze the empirical pdfs of the bed elevation increments, instantaneous Reynolds stress, and the sediment transport rates. We quantify the asymmetry in the pdfs of bed elevation increments and instantaneous Reynolds stress and contrast them with the symmetric pdfs of sediment transport rates. Figure 4a shows the pdfs of the bed elevation increments ($\Delta h(t) = h(t + \Delta t) - h(t)$) at the highest resolution of $\Delta t = 5 \text{ s}$ for the discharges of 1500 l/s, 2000 l/s and 2800 l/s. These bed elevations were sampled at the location of sonar 3 positioned at the downstream end of the channel (see Figure 1b). As can be seen from the figure, the width of the pdf increases with increasing discharge and the pdf becomes more skewed to the right indicating a higher chance of finding high positive bed elevation increments, $h(t + \Delta t) - h(t) > 0$ in the time-evolving bed.

[16] Figure 4b shows the pdfs of the normalized instantaneous Reynolds stresses, for the discharges of 1500 l/s, 2000 l/s and 2800 l/s, respectively. The normalized instantaneous Reynolds stresses were computed as:

$$\tau_{u'w'}^* = \frac{-\rho_w u' w'}{(\rho_s - \rho_w) g d_{50}}, \quad (2)$$

where u' are the mean-removed longitudinal velocity fluctuations, w' are the mean-removed vertical velocity fluctuations, ρ_w is the density of water (assumed as 1000 kg/m^3), ρ_s is the density of the dry sediment (assumed as 2650 kg/m^3) and g is the acceleration due to gravity (assumed as 9.81 m/s^2). As can be seen from Figure 4b, the pdfs of instantaneous Reynolds stress look highly asymmetric and are in close agreement with those of the bed elevation increments. However, the pdfs of the increments of the 5 min averaged sediment transport rates for the discharges of 1500 l/s, 2000 l/s and 2800 l/s, shown in Figure 4c, do not seem to display much asymmetry. Below we apply rigorous metrics to quantify the asymmetric nature of the pdfs and how it changes with discharge.

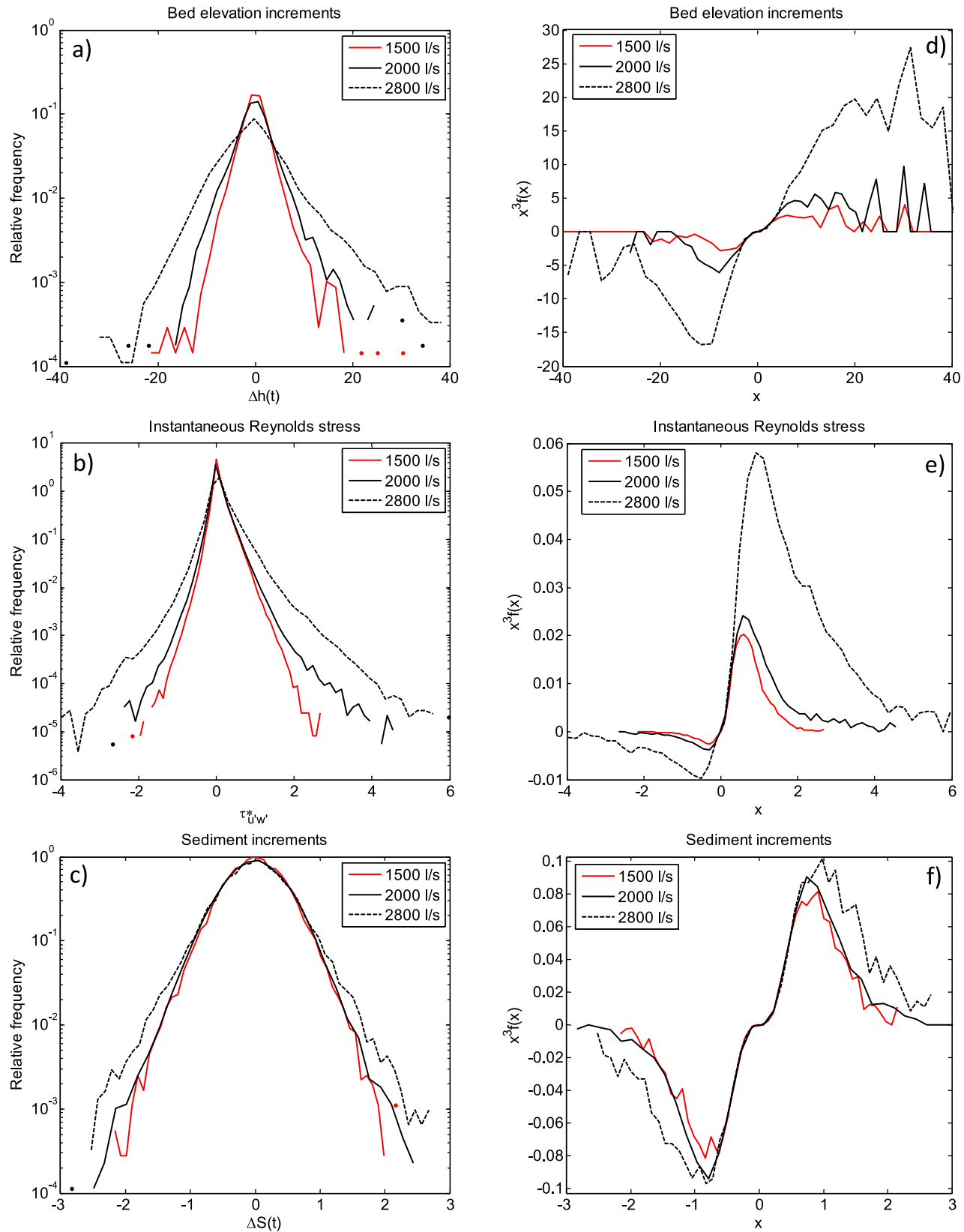


Figure 4. (left) (a) Semilog pdfs of bed elevation increments, (b) instantaneous Reynolds stress, (c) sediment transport increments, and (right) their third moment functions ($x^3 f(x)$, where x is $\Delta h(t)$, τ_{uw}^* and $\Delta S(t)$ in subplot of Figures 4d, 4e and 4f, respectively), for the discharges of 1500 l/s, 2000 l/s and 2800 l/s. Note that all pdfs were computed at the highest resolution, i.e., 5 s for the bed elevations increments, 200 Hz for the instantaneous Reynolds stress and 5 min for the sediment transport increments.

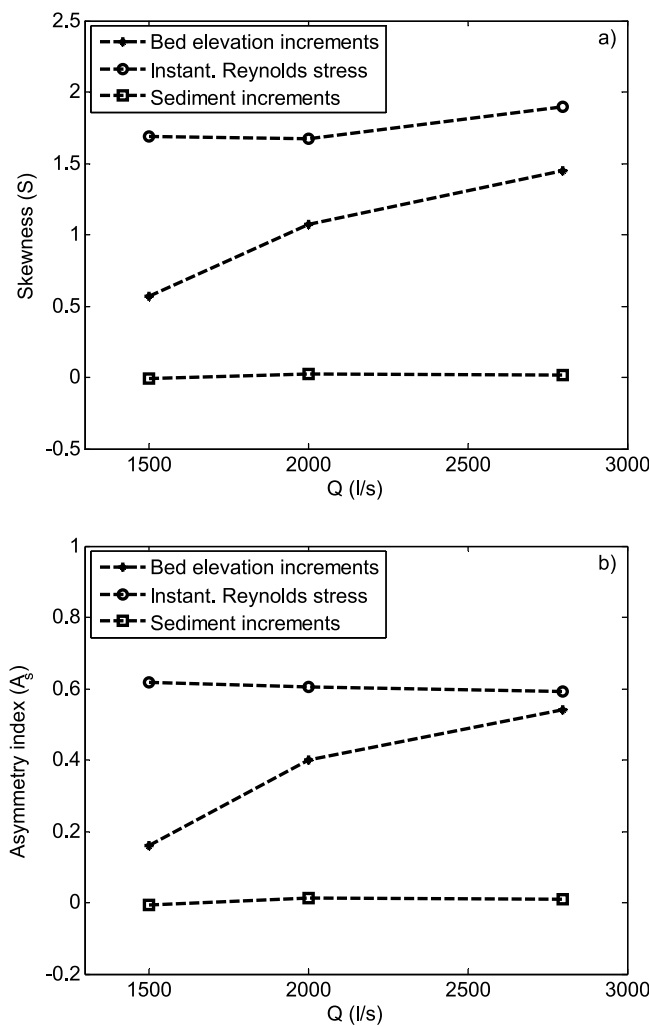


Figure 5. (a) Skewness coefficient and (b) asymmetry index as a function of discharge.

[17] Metrics for quantifying asymmetry around the mean include the coefficient of skewness (S) and the asymmetry index (A_S) defined as:

$$S = \frac{\langle (X - \bar{X})^3 \rangle}{\langle (X - \bar{X})^2 \rangle^{3/2}} \quad (3)$$

$$A_S = \frac{\langle (X - \bar{X})^3 \rangle}{\langle |(X - \bar{X})^3| \rangle} \quad (4)$$

where X is the random variable and \bar{X} is the mean of X . These quantities were computed for bed elevation increments, instantaneous Reynolds stress and sediment transport increments and are shown in Figure 5 for different discharges. As expected from the visual inspection of the pdfs in Figure 4, the bed elevation increments and instantaneous Reynolds stress indeed display significant asymmetry around the mean (observe the non-zero values of S and A_S in Figures 5a and 5b) while the sediment transport increments show a symmetry around the mean. It is also observed from

Figures 5a and 5b that the asymmetry indices of the bed elevation increments clearly increase with increasing discharge while those of the instantaneous Reynolds stress remain almost constant. This is in contradiction with the visual inspection of Figure 4b which indicates an increase of the asymmetry of the tails of the distribution as the discharge increases. Why is it that the skewness coefficient and the asymmetry index are not able to capture this changing asymmetry? The answer lies on the fact that both these indices evaluate the asymmetry of a pdf around the mean; if the mean does not coincide with the mode (most frequently occurring value), as is the case for the instantaneous Reynolds stress which has the mode at zero but a slightly positive mean, then the asymmetry indices S and A_S are not able to differentiate between the effect of a changing mean versus that of a changing tail shape, as the discharge increases. (Note that the empirically computed mean instantaneous Reynolds stresses for the discharges of 1500 l/s, 2000 l/s and 2800 l/s are 0.0681, 0.0719 and 0.1134, respectively, and are very similar to the estimates obtained for the bed shear stress using equation (1) (see Table 1)). To be able to remove the effect of the non-zero mean and evaluate the tail asymmetry as it changes with increasing discharge one has to employ a metric that evaluates higher order moments locally (instead of globally as the indices S and A_S do). This can be done by computing the odd moment functions of $f(x)$ as $x^3 f(x)$ or $x^5 f(x)$ [e.g., see Warhaft, 2002]. Such plots are shown in Figure 4 (right). For example, Figure 4d shows the third moment function of the bed elevation increments, whereas, Figure 4e shows the same for the normalized instantaneous Reynolds stress, clearly depicting the highly asymmetric nature of the pdfs and the amplification of this asymmetry with increasing discharge.

[18] To the best of our knowledge, the asymmetry in the pdfs of the bed elevation increments has not been quantified before in the literature except in Aberle and Nikora [2006], who worked with mean-removed bed elevations over a plane armored bed, and not with bed elevation increments over a bed form dominated gravel bed as done in our study. They documented a similar trend, that is, a change in the shape of the pdf and an increasing asymmetry with increasing discharge. They related the grain size distribution of the bed surface to the standard deviation of the bed elevation series and the asymmetry of the pdfs to the armoring effect. More recently, the asymmetry in the pdfs of bed elevation increments was noted in Singh et al. [2011] but it was not formally quantified.

[19] In contrast to the pdfs of the bed elevation increments and instantaneous Reynolds stress, the pdfs of sediment transport increments show symmetric behavior for all discharges, although the spread of the pdfs increases with increasing discharge (Figures 4c and 4f). The symmetric behavior of the pdfs of sediment transport increments is due to the fact that sediment transport is an integrated quantity (averaged over 5 min) which integrates over the short-lived high magnitude sediment flux pulses produced by the large magnitude asymmetric bed elevation increments (documented above at the resolution of 5 s). Note that the positive values ($\Delta h > 0$) in the increments of the bed elevation correspond to depositional pulses and negative values ($\Delta h < 0$) to erosional pulses, and as such, they are expected to balance each other rendering the integral of the pdfs in the left and

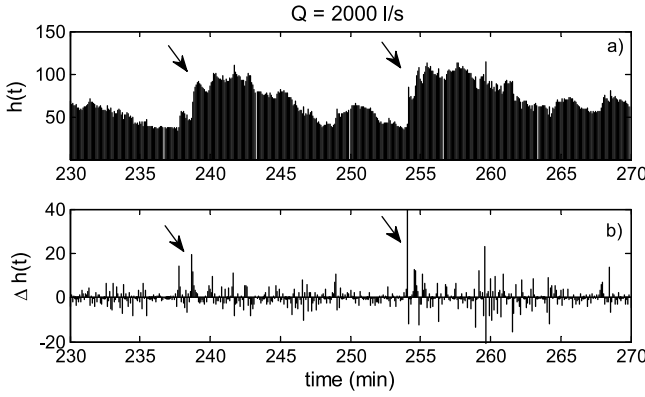


Figure 6. (a) Zoomed-in time series of bed elevation (see Figure 2a) and, (b) its increments for the discharge of 2000 l/s. Arrows indicate large temporal bed elevation increments corresponding to the sharp fronts of the passing bed forms.

right sides of the mean equal, something that was verified in our study). Note also that the large positive temporal elevation increments are associated with the steep fronts of the passing bed forms (Figures 6a and 6b).

3.3. Parameterizing Tail Behavior of Bed Elevation Increments and Instantaneous Reynolds Stress

[20] Along with the asymmetry documented in the previous section, it is noted that the pdfs of the bed elevation increments exhibit concave-up decay in their tails (both in the right and left tails) indicating a tail behavior considerably different than that of a Gaussian pdf (Figures 4a, 7a, and 7b). To further investigate the tail behavior of the pdfs of bed elevation increments, the probability of exceedance for both the positive and negative parts of the pdfs (Figure 4a) were computed separately and are shown in Figures 7a and 7b. These figures suggest a power law tail behavior both in the positive and negative parts of the bed elevation increment pdfs.

[21] A common distribution with a power law decay is a Pareto distribution whose probability density function can be expressed as:

$$f(x) = \alpha \frac{\gamma^\alpha}{x^{\alpha+1}}; \quad x \geq \gamma \quad (5)$$

where α is the tail index, γ is the minimum possible value of the random variable x , also known as the lower bound of the distribution. The probability of exceedance of a Pareto distribution is given by:

$$P(X > x) = \left(\frac{\gamma}{x}\right)^\alpha; \quad x \geq \gamma \quad (6)$$

In many natural systems, however, such as in the case of bed elevations considered here, there is typically a physically-imposed upper bound that truncates the tail of the pdf. In this case, the truncated Pareto distribution is a more appropriate choice. This distribution is given as:

$$f(x) = \frac{\alpha \gamma^\alpha x^{-\alpha-1}}{1 - (\gamma/\nu)^\alpha}; \quad x \leq \nu \quad (7)$$

and its probability of exceedance can be expressed as:

$$P(X > x) = \frac{\gamma^\alpha (x^{-\alpha} - \nu^{-\alpha})}{1 - (\gamma/\nu)^\alpha}; \quad x \leq \nu \quad (8)$$

where ν is the truncation parameter also called upper bound on the random variable, α is the tail index and γ is the lower bound on the random variable X .

[22] To estimate the parameters of the Pareto and truncated Pareto distributions the method of maximum likelihood estimation (MLE) proposed by *Aban et al.* [2006] and *Clauset et al.* [2009] was used in this study. This estimation involves the conditional MLE based on the $(r + 1)$ largest-order statistics representing only the portion of the tail where the truncated Pareto approximation holds. Consider a random sample $X = X_1, X_2, \dots, X_n$ and let $X_{(1)} \geq X_{(2)} \geq \dots \geq X_{(n)}$ denote its ordered statistics, where $X_{(r)}$ is the r th largest observation. The conditional MLE for the parameters of the truncated Pareto distribution based on the $(r + 1)$ largest-order statistics is given by $\hat{\nu} = X_{(1)}$, $\hat{\gamma} = r^{\frac{1}{\alpha}} (X_{(r+1)})[n - (n - r)(X_{(r+1)}/X_{(1)})^{\hat{\alpha}}]^{-1/\hat{\alpha}}$, and $\hat{\alpha}$ is obtained by solving the equation

$$\frac{r}{\hat{\alpha}} + \frac{r(X_{(r+1)}/X_{(1)})^{\hat{\alpha}} \ln(X_{(r+1)}/X_{(1)})}{1 - (X_{(r+1)}/X_{(1)})^{\hat{\alpha}}} = \sum_{i=1}^r [\ln X_{(i)} - \ln X_{(r+1)}]. \quad (9)$$

[23] For a data set that graphically exhibits a power law tail, *Aban et al.* [2006] proposed an asymptotic level- q test ($0 < q < 1$) which rejects the null hypothesis $H_0: \nu = \infty$ (Pareto distribution) if and only if $X_{(1)} < [nC(-\ln q)]^{1/\hat{\alpha}}$, where $C = \gamma^\alpha$. The corresponding p value is given by $p = \exp(-nCX_{(1)}^{-\alpha})$. They proposed the use of Hill's estimator,

$$\hat{\alpha}_H = \left[r^{-1} \sum_{i=1}^r [\ln X_{(i)} - \ln X_{(r+1)}]^{-1} \right], \quad \text{and} \quad (10)$$

$$\hat{C} = \frac{r}{n} (X_{(r+1)})^{\hat{\alpha}_H} \quad (11)$$

for the estimation of the parameters C and α . Note that a small value of $p < 0.1$, indicates a small significance level in accepting the hypothesis that the data set comes from a Pareto distribution (as suggested by *Clauset et al.* [2009]). For more details about the proofs and the method for parameter estimation the reader is referred to *Aban et al.* [2006] and *Ganti et al.* [2011].

[24] Figures 7c and 7d show the fitted Pareto and truncated Pareto distribution for both the positive increments (Figure 7c) and negative increments (Figure 7d) as a function of discharge. The estimated p -values for positive increments for the discharges of 1500 l/s, 2000 l/s and 2800 l/s are 0.0066, 0.0024 and 0.0005, respectively, while for the negative increments are 0.0092, 0.004 and 0.0011. Based on the estimated p -values ($p < 0.1$) we rejected the Pareto distribution for the bed elevation increments at all discharges. While no similar rigorous tests exist for hypothesis testing of the truncated Pareto distribution, the more realistic assumption of the existence of an upper bound and visual inspection of the fitted pdfs (Figures 7c and 7d), led us to accept the truncated Pareto distribution as a reasonable fit to our data.

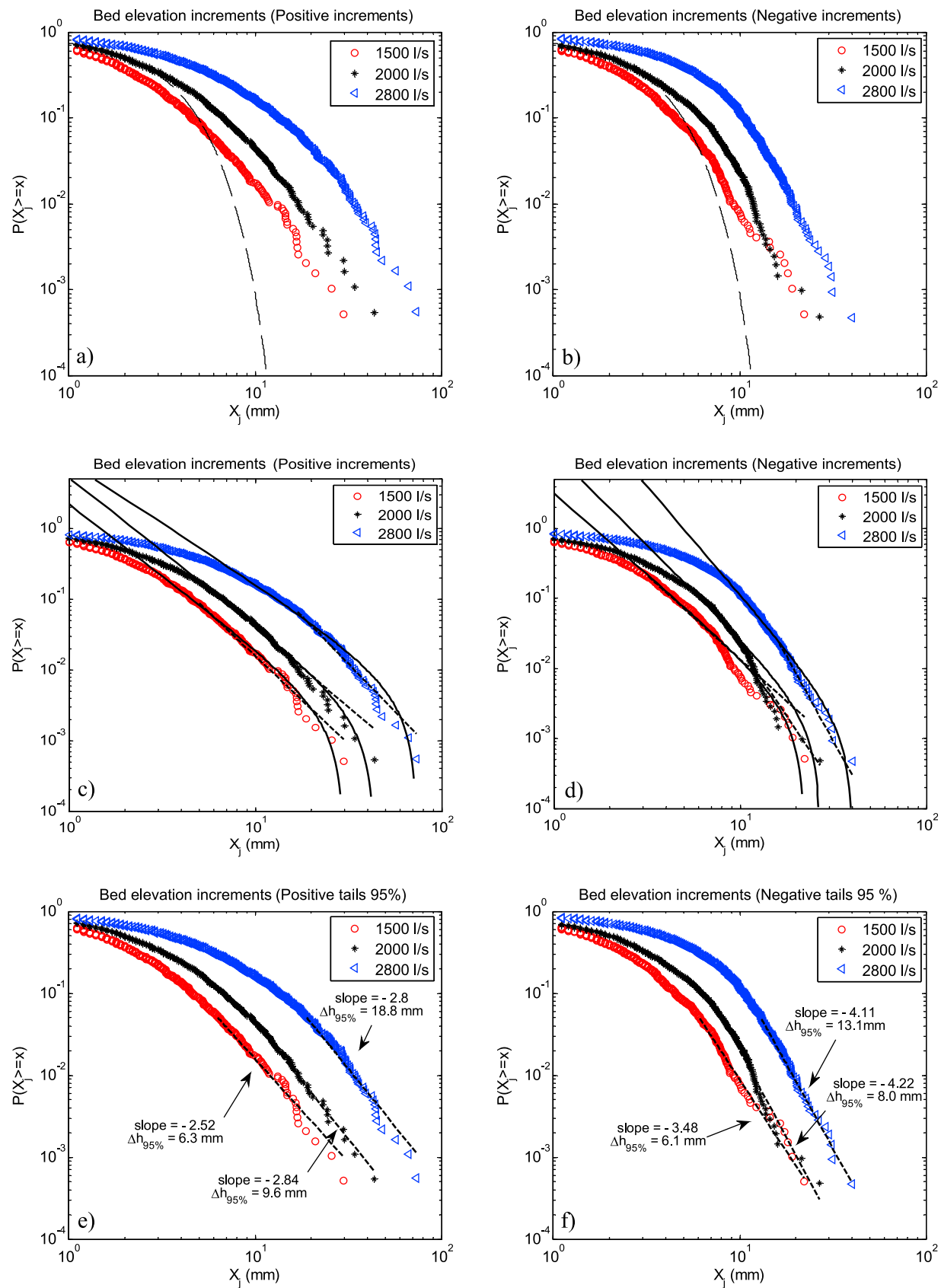


Figure 7

Table 2. Estimated Parameters of the Truncated Pareto and the Pareto Distribution for the Positive [Negative] Increments of the Temporal Bed Elevation Series^a

Q (l/s)	Truncated Pareto Distribution			Pareto Distribution		95 Percentile	
	α	Lower Bound (γ) (mm)	Upper Bound (ν) (mm)	α	Lower Bound (γ) (mm)	α (Pareto Distribution)	$\Delta h_{95\%}$ (mm)
1500	2.09 [2.40]	1.03 [1.21]	29.7 [22.1]	2.49 [2.40]	5.0 [3.2]	2.52 [3.48]	6.3 [6.1]
2000	2.08 [2.65]	1.54 [2.09]	43.5 [26.9]	2.24 [3.91]	5.3 [7.0]	2.84 [4.22]	9.6 [8.0]
2800	1.73 [3.10]	2.22 [4.05]	73.4 [40.0]	2.70 [4.82]	16.9 [16.2]	2.8 [4.11]	18.8 [13.11]

^aAlso shown are the Pareto distribution parameters fitted to the tails exceeding the upper 95% quantile ($\Delta h > \Delta h_{95\%}$).

[25] Table 2 shows the estimated parameters of the fitted Pareto and truncated Pareto distributions for the discharges of 1500 l/s, 2000 l/s and 2800 l/s for both positive and negative increments. The upper bounds on the truncated Pareto pdfs for the positive increments for the discharges of 1500 l/s, 2000 l/s and 2800 l/s were found to be 29.7 mm, 43.5 mm and 73.4 mm, respectively (Table 2). It is interesting to note that these values, statistically estimated from the data, are close to the independently estimated maximum bed elevation increments for the corresponding discharges.

[26] Comparing the tail parameter (α) of the pdfs of the positive and negative increments of the bed elevation series (see Table 2), it can be seen that the tail in the positive increments is heavier (smaller α values) than that in the negative increments for all discharges considered in this study. This can be seen as another way of quantifying the asymmetry in the pdfs of the bed elevation increments. Moreover, this difference indicates that the underlying dynamics, for example, resulting from the physical mechanisms of grain sorting by entrainment, transport, and deposition, is different in the stoss (mostly negative increments corresponding to erosion) versus lee side (mostly positive increments corresponding to deposition) of a bed form, with a smaller chance of extreme erosional events compared to depositional events of the same magnitude.

[27] To further understand the nature of the probabilistic truncation in the pdfs of bed elevation increments, the upper tails (bed elevation increments exceeding the 95 percentile $P(X > x_{95\%})$) of both the positive and negative bed elevation increments were investigated. From Figures 7e and 7f it can be seen that the upper tails (probability of exceedance $>95\%$) of the pdfs of bed elevation increments decay in a manner well approximated by a power law with exponent of ~ -2.7 for positive increments (Figures 7e) and ~ -4 for negative increments (Figure 7f). These values of α are higher compared to the estimated values of α for the truncated Pareto pdfs (see Table 2) implying that at high exceedance probabilities the tails become “thinner”, i.e., display an almost exponential decay. Such a behavior is indicative of a “soft thresholding”, suggesting that the whole pdf could be well approximated by a tempered Pareto distribution, i.e., a truncated Pareto distribution

whose truncation level is itself an exponentially distributed random variable [e.g., Meerschaert et al., 2012]. Such a fitting has not been pursued in the present study.

[28] A similar analysis was performed for the instantaneous Reynolds stress. For example, Figure 8 shows a log-log plot of the probability of exceedance of the positive tails of the instantaneous Reynolds stress indicating a good approximation by a power law decay. The parameters of the fitted Pareto distribution for these positive tails are shown in Table 3. It can be seen that the fitted values of α are much higher than the corresponding values for the bed elevation increments, indicating a faster decay (“thinner tails”) in the instantaneous Reynolds stress, which however still exhibit a tendency to become thicker with increasing discharge.

4. Multiscale Statistics of Bed Topography

[29] Bed topography exhibits variability over a broad range of spatial scales: from the grain size to bed form size. This spatial variability is expected to manifest itself in the temporal series as well and this is visually observed in Figure 2a where small scales are seen superimposed on larger scales. A common way to characterize variability across a range of scales is via computing the power spectral density (hereafter PSD). The PSDs of the bed elevation series are shown in Figure 9 for the discharges of 1500 l/s (Figure 9a), 2000 l/s (Figure 9b) and 2800 l/s (Figure 9c). From Figure 9 it can be seen that the PSDs follow a power law as a function of frequency or timescale (1/frequency) for all the discharges suggesting the presence of statistical scale invariance (scaling) in the bed elevation series, at least within a range of scales. It is interesting to note that with increasing discharge the slope of the PSD increases (see Table 4 for the slopes and scaling regimes of PSDs of bed elevation for the discharges of 1500 l/s, 2000 l/s and 2800 l/s). For example, the slope of the PSD at the discharge of 1500 l/s is ~ 1.87 and increases to ~ 2.18 at the discharge of 2800 l/s. Also, as the discharge increases, the largest timescale (i.e., the timescale of the largest bed form present in the series) decreases. For example, the bed form timescale for the case of 1500 l/s is ~ 55 min, ~ 40 min for 2000 l/s, and ~ 25 min for 2800 l/s. This is expected due to

Figure 7. Log-log plot of the probability of exceedance for the (a) positive bed elevation increments, and (b) the negative bed elevation increments with the Gaussian distribution displayed in broken line. Fitted truncated Pareto (solid line) and Pareto distribution (dotted line) to (c) positive increments and (d) negative increments. (bottom) The fitted Pareto distribution to the values exceeding the 95 percentile of the (e) positive tails and (f) negative tails. The estimated parameters of these distributions are summarized in Table 2. Note that the x-axes in the right column plots represent absolute values of negative bed elevation increments.

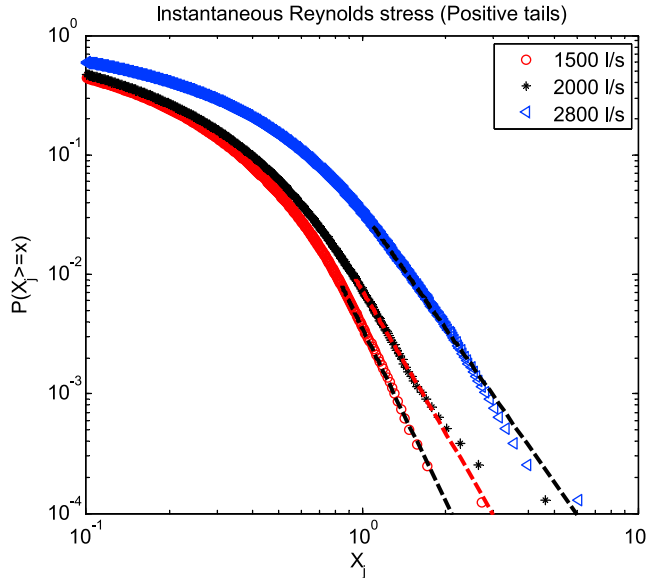


Figure 8. Log-log plot of the probability of exceedance for the positive tail of instantaneous Reynolds stress distributions with fitted Pareto distribution. The estimated parameters of these distributions are summarized in Table 3.

the faster overall movement of the largest bed forms with increasing discharge, as also documented in *Singh et al.* [2011].

[30] The increasing spectral slope with increasing discharge (see Table 4) in the spectra of the temporal bed elevation suggest that bed forms of comparable energy (height) move faster at higher discharge. This finding is consistent with the results reported in *Singh et al.* [2011] where the scale-dependent celerity of bed forms at two different discharges (2000 l/s and 2800 l/s) were compared [see, e.g., *Singh et al.*, 2011, Figures 12c and 12d] and a higher celerity of the largest bed form as well as a higher decay rate of celerity with scale was reported at higher discharge.

[31] It is important to note that the PSD characterizes how the second order moment (variance) in the signal changes with scale/frequency and, as such, it fully characterizes only the evolution of a Gaussian pdf over scales. Since the pdfs of the bed elevation increments show significant deviation from the Gaussian distribution (see above sections), it is important to test the presence of scaling in the higher order statistical moments. For this, we used higher order structure function analysis which quantifies the manner in which higher order statistical moments of the local increments in the bed elevation series change with scale. In particular, a statistical analysis was performed on the increments of the bed elevation time series $h(t)$ at different scales a , denoted by $\Delta h(t, a)$, and defined as:

$$\Delta h(t, a) = h(t + a) - h(t) \quad (12)$$

where t is the time and a is the scale. Note that while $h(t)$ is always positive (since $h(t)$ is computed with reference to the lowest bed elevation i.e., the global minimum), the increments $\Delta h(t, a)$ can be both positive and negative; in fact, their mean value is zero. The q th order statistical moment

estimates of the absolute values of the increments at scale a , also called the partition functions or structure functions, $M(q, a)$, are defined as:

$$M(q, a) = \frac{1}{N} \sum_{t=1}^N |\Delta h(t, a)|^q \quad (13)$$

where N is the number of data points of the series at scale a . If a series shows statistical scaling (i.e., scale-invariance), $M(q, a)$ is a power law function of the scale a , that is:

$$M(q, a) \sim a^{\tau(q)} \quad (14)$$

where $\tau(q)$ is called the scaling exponent function. The most basic form of scaling, known as simple scaling or mono-scaling, occurs when the scaling exponents are a linear function of the moment order i.e., when $\tau(q) = Hq$. In this case, the single parameter H describes how the whole pdf changes over scale. Notice that in this case H relates to the spectral slope β as $H = (\beta - 1)/2$. A small Hurst exponent $H < 0.5$ indicates anti-correlation and thus a very rough signal, while $H > 0.5$ indicates long-range dependence and thus a smoother overall signal [Saupe, 1988]. This ‘smoothness/roughness’ is a global property of the signal and does not capture the possible local variations in the degree of roughness. If $\tau(q)$ is nonlinear, more than one parameter is required to describe how the behavior of the pdf changes over scale [e.g., *Castaing et al.*, 1990; *Venugopal et al.*, 2006] and the series is called a multifractal. For many processes the non-linear relationship of $\tau(q)$ with q can be parameterized as a polynomial, with its simplest form as a quadratic approximation [*Venugopal et al.*, 2006]:

$$\tau(q) = c_1 q - \frac{c_2}{2} q^2 \quad (15)$$

Multiscale analysis in this framework provides a simple way, using only two parameters c_1 and c_2 , of parameterizing the change of the pdf over a range of scales. The parameter c_1 is a measure of the average “roughness” of the series (akin to H), while c_2 , called the intermittency parameter, gives a measure of the statistical variability of the local roughness, i.e., the degree of heterogeneity in the temporal arrangement of the local abrupt fluctuations in the series. For more details about such an analysis see *Singh et al.* [2011].

[32] Figure 10a shows the structure functions of bed elevations monitored at sonar 3 for the discharge of 2000 l/s. The scaling range (the range of scales where the structure functions show log-log linearity) is of the order of 0.5–10 min, while the previously estimated largest scale of the bed form is of the order of 40 min (see Table 4).

Table 3. Estimated Parameters of the Pareto Distribution Fitted to the Positive Tails of the Instantaneous Reynolds Stress

Q (l/s)	α	Lower Bound (γ)
1500	4.79	0.84
2000	3.95	0.94
2800	3.25	1.09

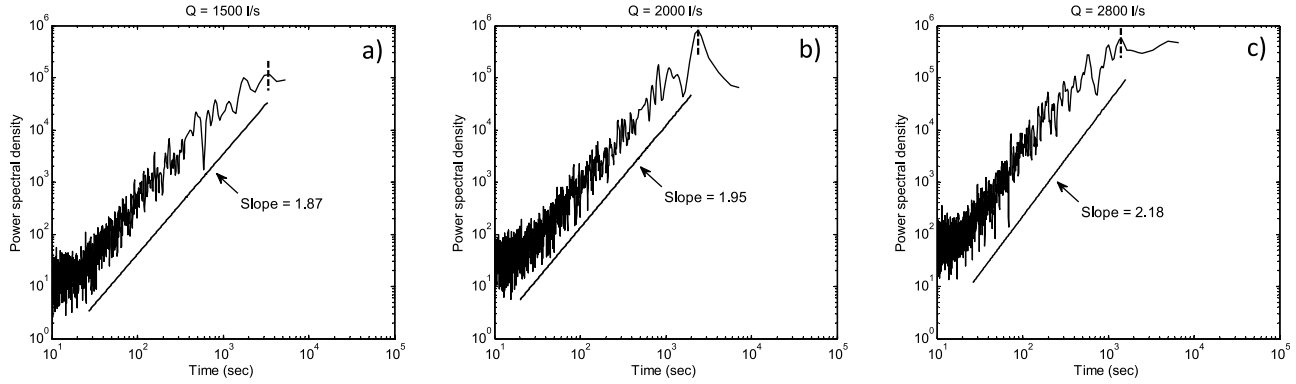


Figure 9. Power spectral density (PSDs) of temporal bed elevation series for the discharge of (a) 1500 l/s, (b) 2000 l/s and (c) 2800 l/s. Note that the vertical dotted lines in the PSDs correspond to the largest scale (bed form) present in signal. Also note that the units of the PSDs of the bed elevation is $\text{mm}^2/\text{s}^{-1}$ (quantity $^2/\text{freq}$).

[33] We observe that the $\tau(q)$ curve has a nonlinear dependence on q , which is an indication of the presence of multifractality (Figure 10b). Note that for brevity we have plotted the structure functions and $\tau(q)$ curve for the bed elevations sampled at probe 3 for the discharge of 2000 l/s only. For the other discharges, the multifractal parameters are given in Table 4. From Table 4, it can be seen that the roughness coefficient c_1 along with the intermittency coefficient c_2 increased with increasing discharge.

[34] That the roughness parameter c_1 increases with increasing discharge suggests that bed elevation fluctuations are smoother overall (strong temporal persistence) at higher discharge than at lower discharge, as also found in Singh et al. [2009a]. The increase of c_2 with increasing discharge suggests that sharp elevation increments due to the passing steep bed forms or sub-bed form facies are not homogeneously arranged in the signal (partly due to the fact that bed forms of a wider range of sizes are present at higher discharges).

5. Physical Interpretation of the Asymmetry in Instantaneous Reynolds Stress Distribution

[35] In section 3.2 we characterized the asymmetry in the pdfs of the bed elevation increments and how this asymmetry grows as a function of discharge. In this section we focus on the signature of turbulent velocities and bed elevation fluctuations on the instantaneous Reynolds stress. We note that the extreme values of instantaneous Reynolds stress fluctuations result from large fluctuations in the longitudinal velocity (u) and/or vertical velocity (w). A common way to quantify the contribution of each velocity component (u and v) to the turbulent flow field is by

plotting the joint probability distribution of the longitudinal (u') with vertical (w') velocity fluctuations, obtained by removing their respective mean from the velocity series. These plots are also called quadrant plots [Lu and Willmarth, 1973; Bennett and Best, 1995; Nelson et al., 1995; Buffin-Bélanger et al., 2000; Best, 2005; Hardy et al., 2009, 2010] and are shown in Figure 11 for the discharges of 1500 l/s (Figure 11a), 2000 l/s (Figure 11b) and 2800 l/s (Figure 11c).

[36] In quadrant plots, four regions of distinct fluid motion characteristics with respect to the mean flow are differentiated. Quadrant I (Q_{D1}) where $u' > 0$ and $w' > 0$, represents outward interaction; Quadrant II (Q_{D2}) where $u' < 0$ and $w' > 0$, represents ejection; Quadrant III (Q_{D3}) where $u' < 0$ and $w' < 0$, represents inward interaction; whereas Quadrant IV (Q_{D4}) where $u' > 0$ and $w' < 0$, represents sweep motion [Nelson et al., 1995; Buffin-Bélanger et al., 2000; Best, 2005; Hardy et al., 2009, 2010]. Since instantaneous Reynolds stress is given by $\tau = -\rho u' w'$, quadrant analysis can be used to partition the total Reynolds stress between different velocity components and assess the importance of each in contribution to the sediment transport [Nelson et al., 1995]. For example, Nelson et al. [1995] argued that sweeps, that contribute positively to the instantaneous Reynolds stress, collectively move the majority of sediment since they are extremely common. However, they also mentioned that outward interactions, that contribute negatively to instantaneous Reynolds stress and are relatively rare, individually move as much sediment as sweeps and much more than ejections and inward interactions.

[37] The relative contribution of the instantaneous Reynolds stress to each quadrant can be seen in Figures 11a, 11b, and 11c

Table 4. Multifractal Properties of Temporal Bed Elevation

Q (l/s)	Probe	Spectral Slope	Spectral Scaling Range	Multifractal Parameters		Multifractal Scaling Range
				c_1	c_2	
1500	Probe 3	1.87	15 s–55 min	0.48	0.09	0.5–8 min
2000	Probe 3	1.95	20 s–40 min	0.53	0.12	0.5–10 min
2800	Probe 3	2.18	20 s–25 min	0.55	0.13	0.5–7 min

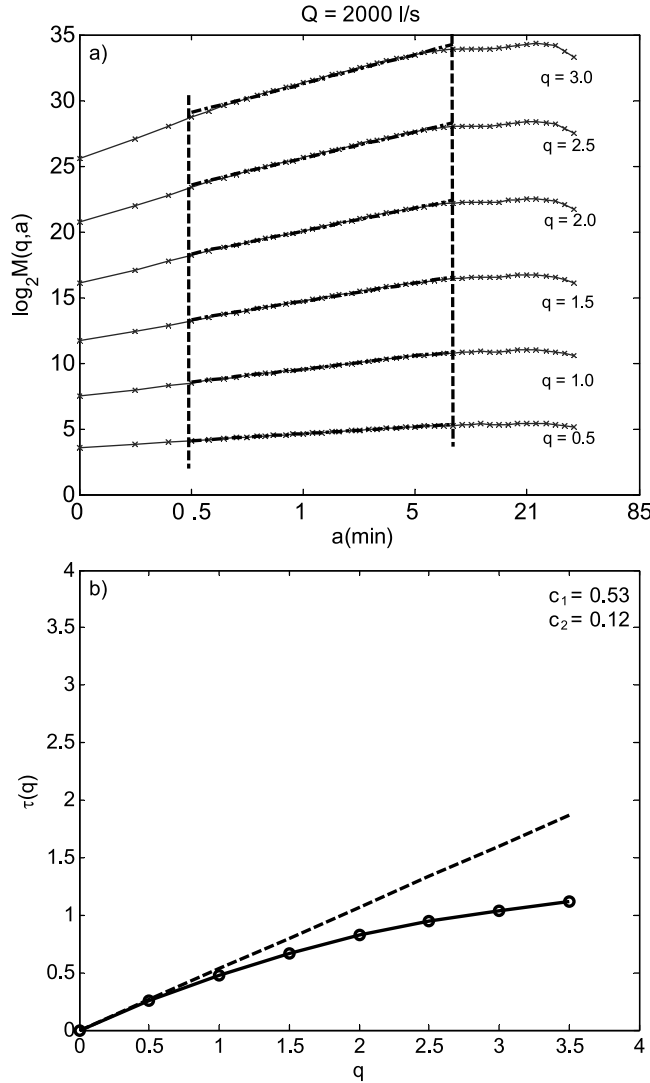


Figure 10. (a) Statistical moments of the increments of the bed elevation time series as a function of scale and (b) the scaling exponents $\tau(q)$ estimated from the log-log linear regressions within the scaling regions. Notice the deviation of $\tau(q)$ from the straight line establishing the presence of multifractality.

for the discharges of 1500 l/s, 2000 l/s and 2800 l/s, respectively. It can be seen that although the mass of the distribution is more concentrated in Q_{D4} , the scatter of the joint distribution of velocity fluctuations is higher in Q_{D2} and increases with increasing discharge. This scatter can be well described by fitting an ellipse to the scatterplot. Figure 11d shows the asymmetric growth of the quadrants captured by the best fitted ellipse (fitted using least squares error) as a function of discharge. Notice that the scatter of the velocity fluctuations in Q_{D2} increases with increasing discharge leading to anisotropic growth of the ellipse as a function of discharge. We suggest that the higher scatter in the velocity fluctuations in Q_{D2} is due to the presence of prominent topography (higher bed forms), which increases as the bed form height increases. These higher bed forms create more space for ejection events.

In contrast to the bed with pronounced bed forms, in the hypothetical case of plain bed or stationary bed forms, the shape of the ellipse is expected to change symmetrically as a function of discharge.

[38] A complementary way to visualize the contribution of each velocity component (u' , w') in each quadrant is by plotting their conditional probability distributions as shown in Figure 12. Figures 12a and 12b show the conditional pdfs of the longitudinal (vertical) velocity fluctuations as a function of discharge. Notice that although the evolution of the conditional pdf in each quadrant follows a similar trend, with increasing discharge (and evolving topography), conditional extremes can be easier identified, as the chance of finding a higher positive value of w' is much higher in Q_{D2} .

[39] It is worth noting that the standard deviation of both u' and w' is higher in Q_{D2} compared to Q_{D1} , Q_{D3} and Q_{D4} and it increases with increasing discharge (see Table 5). Also, the correlation coefficient computed between u' and w' follows a similar trend, i.e., it is higher in Q_{D2} as compared to Q_{D1} , Q_{D3} and Q_{D4} , though negatively correlated, and increases with increasing discharge. However, the joint contribution of u' , w' to the Q_{D2} decreases slightly with increasing discharge (see Figures 11a, 11b, and 11c). For example, u' , w' contribute 31.35% of the total mass to the pdf to Q_{D2} for the discharge of 1500 l/s, 30.89% for the discharge of 2000 l/s and 29.42% for the discharge of 2800 l/s. Considering the evolution of the pdf as a function of discharge for both negative and positive sides, the mass in the negative side of the pdf increases with increasing discharge (35.92%, 36.79% and 37.45% for the discharges of 1500 l/s, 2000 l/s and 2800 l/s, respectively) whereas the mass in the positive side decreases with increasing discharge (64.08%, 63.21% and 62.55% for the discharges of 1500 l/s, 2000 l/s and 2800 l/s, respectively).

6. Scale-to-Scale Interaction of Bed Elevation and Instantaneous Reynolds Stress

[40] In the previous sections we computed the marginal statistics of bed elevation, instantaneous Reynolds stress, and sediment transport at the resolution of our measurements. We discussed the physical reasoning for the presence of asymmetry in the distributions of bed elevation increments and instantaneous Reynolds stress. In this section, we wish to examine the scale-to-scale interaction between bed elevation, instantaneous Reynolds stress, and sediment transport rates. Unfortunately, our data do not allow a scale-to-scale interaction analysis between instantaneous Reynolds stress and sediment transport. This is due to the spacing between the measurement location of velocities (ADV) and sediment transport (bedload traps) which is ~ 1.2 m in the flow direction in this case (see schematic of the experimental setup, Figure 1b) and which is too large a distance to expect causative effects. Therefore, we focus on the scale-to-scale correlation analysis of bed elevations with instantaneous Reynolds stresses.

[41] An efficient way to perform such an analysis is via wavelets [e.g., Kumar and Foufoula-Georgiou, 1997; Venugopal et al., 2006]. Wavelets decompose a signal into a suite of signals each one representing the energy (variability) at different scale. On these signals, one can then

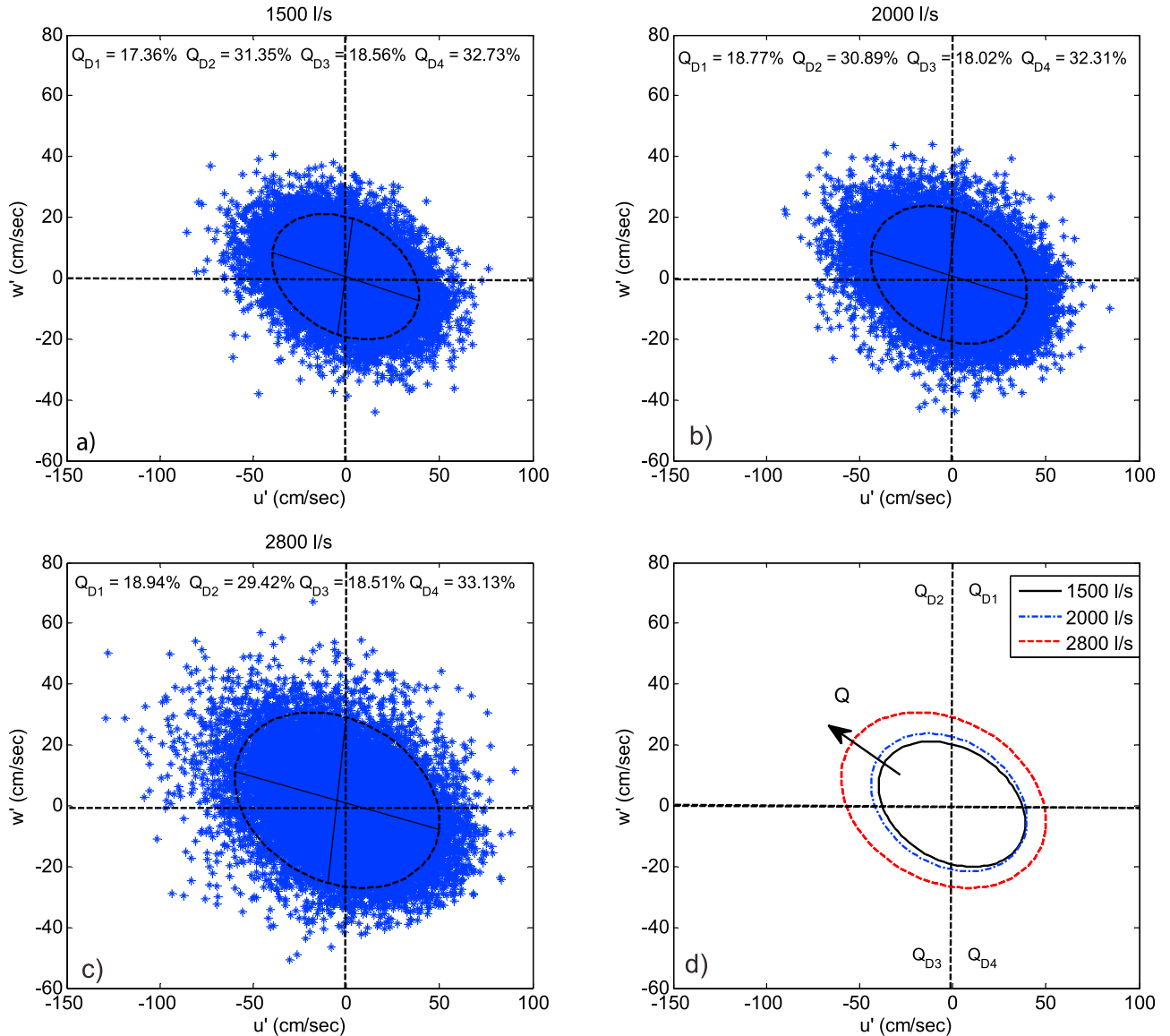


Figure 11. Joint probability distribution of longitudinal (u') and vertical (w') velocity fluctuations obtained by removing their respective mean velocity component for the discharges of (a) 1500 l/s, (b) 2000 l/s and (c) 2800 l/s. The asymmetric growth of the quadrants captured by the best fitted ellipse as a function of discharge is shown in the bottom right plot (Figure 11d). Notice that, although the mass is more concentrated in quadrant 4, the scatter of velocity fluctuations in quadrant 2 becomes more prominent as the discharge increases leading to anisotropic growth of the ellipse as function of discharge.

perform a standard cross-correlation analysis. Wavelets offer localization in both time and frequency and the choice of wavelets in this respect is important. In our analysis we preferred not to use the Haar wavelet (corresponding to simple increments of the process at different scales) as this has poor localization properties in the frequency domain [e.g., *Mallat*, 1998]. Rather, we used the Mexican hat wavelet (second order derivative of the Gaussian function) which is known to possess optimal localization in both time and frequency [*Kumar and Foufoula-Georgiou*, 1997; *Mallat*, 1998; *Singh et al.*, 2009a]. Besides, such a wavelet removes second order polynomial trends from a signal, rendering it stationary for a correlation analysis (for more details the reader is

referred to *Venugopal et al.* [2003] and *Singh et al.* [2011] for a similar analysis).

[42] The wavelet transform of a function $f(t)$ is defined as the integral transform of the function with a series of functions $\psi_{a,b}(t)$, i.e.,

$$W_{f(t)}(a, b) = \int_{-\infty}^{+\infty} f(t) \psi_{a,b}(t) dt \quad (16)$$

where the functions $\psi_{a,b}$ are obtained from the “mother” wavelet $\psi(t)$ by translation and scaling, i.e.,

$$\psi_{a,b}(t) = \frac{1}{\sqrt{a}} \psi\left(\frac{t-b}{a}\right); a > 0; b \in R. \quad (17)$$

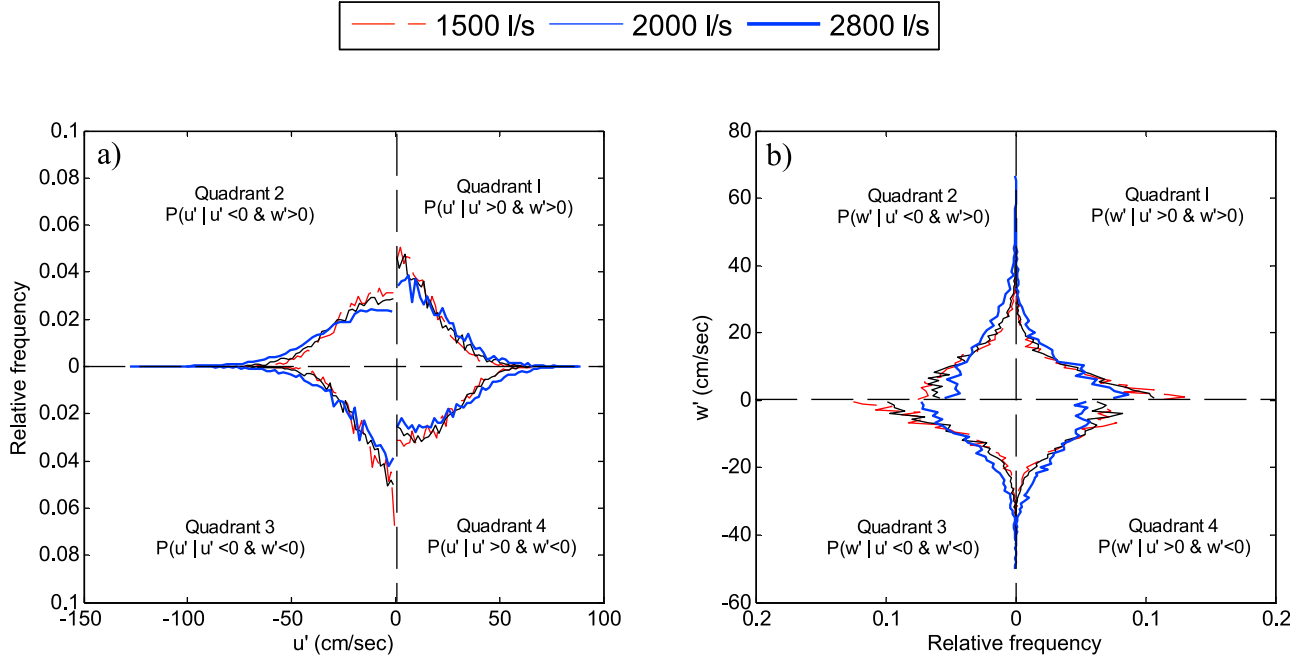


Figure 12. Conditional probability distribution of the (a) longitudinal velocity fluctuations (u') and (b) vertical velocity fluctuations (w') for the discharges of 1500 l/s, 2000 l/s and 2800 l/s. Notice that, with increasing discharge the tails in the pdfs of both the longitudinal and vertical velocity fluctuations become thicker in quadrant 2 as compared to other quadrants.

where a is the scaling parameter and b is the location parameter. The wavelet cross-covariance between two signals $f_1(t)$ and $f_2(t)$ is defined as:

$$WCC_{f_1, f_2}(a, \Delta t) = \int_{-\infty}^{+\infty} W_{f_1}(a, b) W_{f_2}(a, b + \Delta t) db \quad (18)$$

where $W_{f_1}(a, b)$ and $W_{f_2}(a, b)$ are the wavelet coefficients of $f_1(t)$ and $f_2(t)$ respectively at scale a and location b . The wavelet cross-correlation can be obtained by appropriate normalization by the variance of the signals.

[43] As discussed above, in this study, the fluctuations (wavelet coefficients, WC) of bed elevations and instantaneous Reynolds stress at various scales were computed using the Mexican-hat wavelet $g_2(t)$ as the mother wavelet. To test the robustness of our results, we also implemented higher order wavelets g_3 and g_4 without, however, significant change in our results, implying that the chosen Mexican hat wavelet is able to remove non-stationarities present in the signals. To attain the same resolution of instantaneous Reynolds stress time series $\tau_{u'w'}$ as the bed elevation time

series, the $\tau_{u'w'}$ series was downsampled to a resolution of 5 s before performing the cross-correlation wavelet analysis.

[44] Figures 13a and 13c show the wavelet coefficients of the decomposed bed elevation series whereas Figures 13b and 13d show the wavelet coefficients of decomposed instantaneous Reynolds stress series at the scales of 1 min and 6 min, respectively, for a discharge of 2000 l/s. These scales of 1 min and 6 min were arbitrarily chosen from within the scaling range revealed by the structure function analysis of bed elevations (see Figure 10a and Table 4). The maximum cross-correlation obtained between the bed elevation and instantaneous Reynolds stress series at each scale is shown in Figure 14. As expected, with increasing scale the cross-correlation coefficient increases, showing that larger scales are more highly correlated than smaller scales.

[45] A few observations can be made from the plot of Figure 14. First, for very small scales (<5 min) the cross-correlation coefficients are very small (~ 0.2) implying that the linear correlation does not capture the interaction of small scale features of turbulence and bed forms. This may be due to the distance of the velocity sensor (ADV) from the bed. Eddies modulated by the bed and smaller in size than

Table 5. Conditional Statistics of the u' , w' for Different Quadrants for the Discharges of 1500 l/s, 2000 l/s and 2800 l/s

Quadrant	Q = 1500 (l/s)			Q = 2000 (l/s)			Q = 2800 (l/s)		
	$\sigma(u')$ (cm/s)	$\sigma(w')$ (cm/s)	Correlation Coefficient	$\sigma(u')$ (cm/s)	$\sigma(w')$ (cm/s)	Correlation Coefficient	$\sigma(u')$ (cm/s)	$\sigma(w')$ (cm/s)	Correlation Coefficient
Q_{D1}	10.71	5.59	-0.11	11.77	5.97	-0.09	13.70	7.88	-0.06
Q_{D2}	12.98	6.46	-0.18	14.39	7.08	-0.21	18.64	9.58	-0.24
Q_{D3}	10.63	5.28	-0.08	11.77	5.93	-0.08	15.32	7.81	-0.03
Q_{D4}	12.68	6.03	-0.12	12.60	6.41	-0.09	15.49	7.97	-0.11

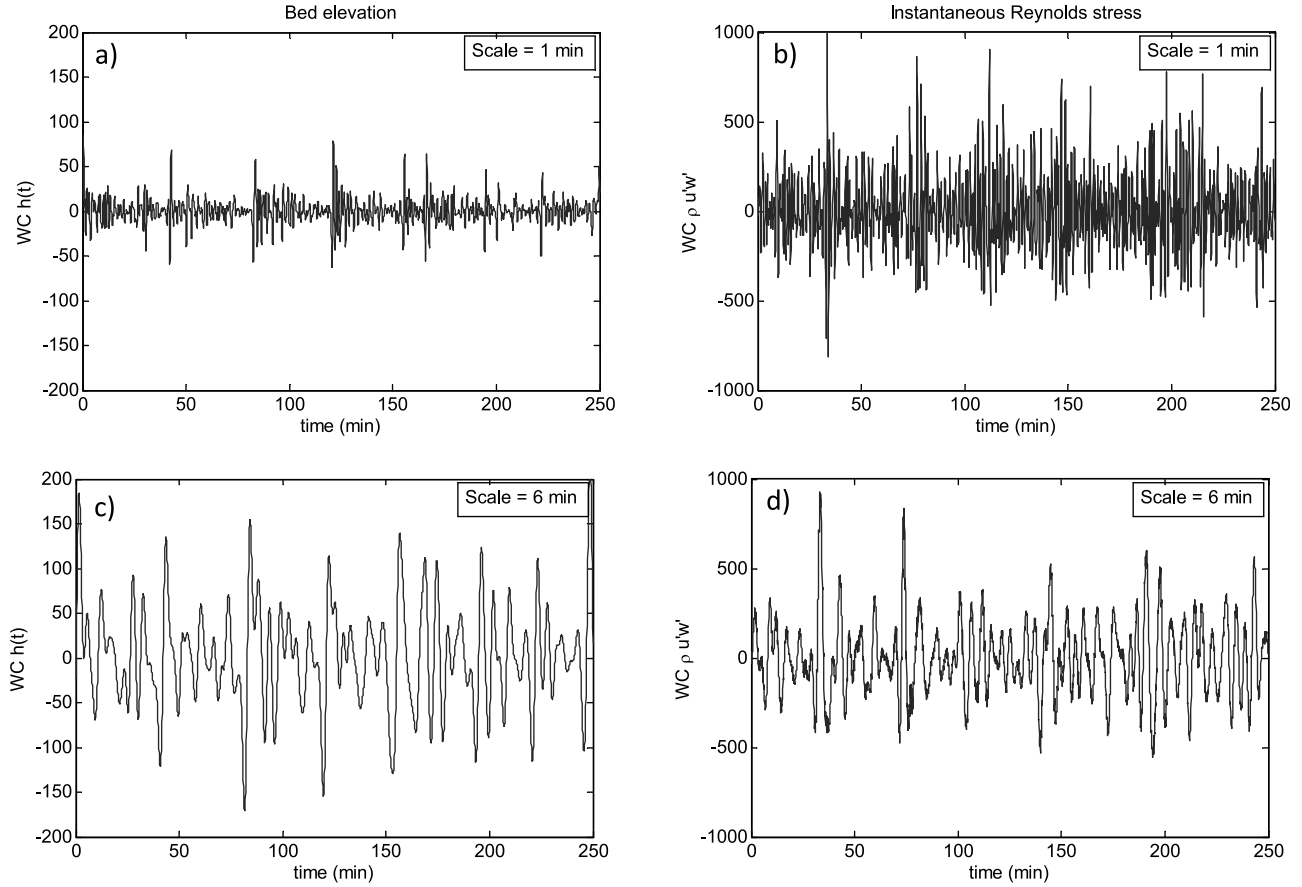


Figure 13. Wavelet coefficients of the (a, c) bed elevation and the (b, d) instantaneous Reynolds stress computed using the Mexican hat wavelet at scales of 1 min (top) and 6 min (bottom) for the discharge of 2000 l/s.

the distance between the sensor and bed will not be detected by the sensor. A closer proximity of the velocity sensor to the bed might have resulted in higher correlation coefficient. For larger scales, (>40 min), the correlation-coefficient is larger (~ 0.7) and statistically significant. It also seems to reach a saturation level (at least for the lower and higher discharges). This observation suggests that linear dependence between bed topography and instantaneous Reynolds stress saturates (becomes maximum) at timescales of about 40 mins and, therefore, integrated quantities at timescales larger than this scale could be used for (scale-independent) predictive modeling of processes such as bedload transport. This is further examined in the next section.

7. Predictive Modeling of Bedload Transport From Instantaneous Reynolds Stress

[46] Prediction of bedload transport from a single flow variable is highly uncertain [Boyer *et al.*, 2006] because the correlation between flow and transport is strongly affected by spatial/temporal inhomogeneities: higher spatial/ temporal inhomogeneities result in lower prediction accuracy. Although many empirical formulas exist in the literature to compute sediment transport rate from total bed shear stress calculated as the product of flow depth h and bed slope S ($\tau = \rho ghS$), these formulas were derived over

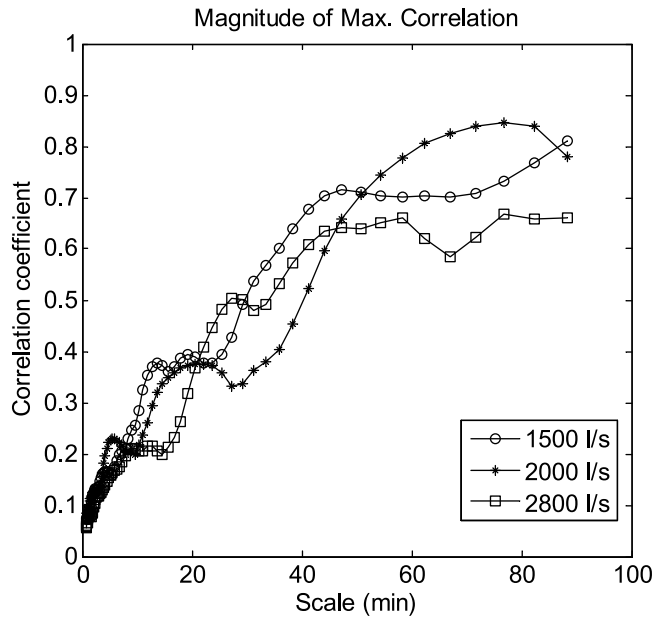


Figure 14. Plot of maximum cross-correlation coefficient obtained between temporal bed elevation and instantaneous Reynolds stress series as a function of scale using wavelet analysis.

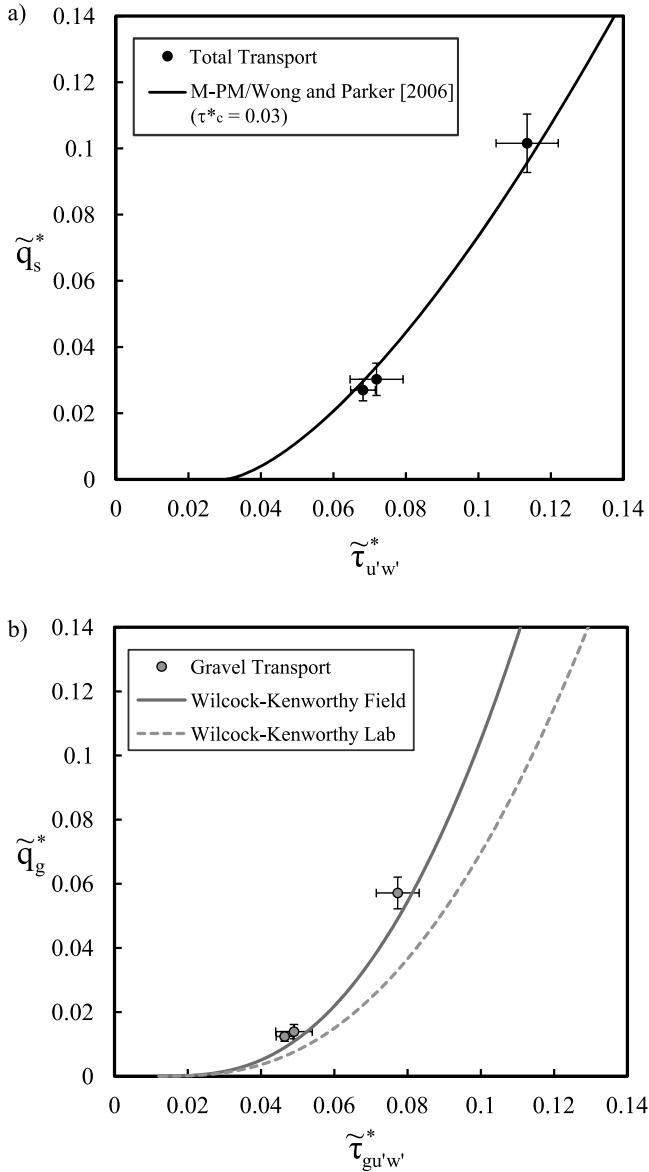


Figure 15. Sediment transport rate as a function of instantaneous Reynolds stress, averaged over bed form time-scales. Error bars indicate the standard deviation about bed form averaged quantities. (a) Total transport rate compared to Meyer-Peter and Müller transport relation as modified by Wong and Parker [2006], using $\tau_c^* = 0.03$. (b) Gravel transport rates (62% to 76% of the total transport rate) compared to Wilcock and Kenworthy relation. Both transport rate and shear stress are made dimensionless using R , g , and grain size.

plane beds [e.g., see Wong and Parker, 2006, and references therein] and have been found inadequate for modeling sediment transport over bed form fields [Nelson et al., 1993; McLean et al., 1994; Nelson et al., 1995; Best, 2005].

[47] For steady uniform flow (e.g., plane bed condition), turbulence can be fully characterized by the local bed shear stress [Nelson et al., 1995; Schmeeckle and Nelson, 2003]. However, for nonuniform flow (e.g., with bed forms) the

total shear stress is divided in two components, skin friction and form drag [see Wiberg and Nelson, 1992, and references therein] and hence in such flows sediment transport modeling generally requires more information than just the total boundary shear stress [Nelson et al., 1995; Sumer et al., 2003].

[48] It was documented earlier that bed elevation fluctuations have a strong linear correlation (corr. coeff. >0.5) with instantaneous Reynolds stress at scales greater than approximately 35 min (Figure 14). These scales correspond to bed form time-scales (e.g., see the saturation time-scales of the PSD of bed elevations in Figure 9). To investigate the relation between sediment transport rates and instantaneous Reynolds stress, we performed a filtering of the sediment transport rate series and the instantaneous Reynolds stress series via a moving window of size 35 min to 60 min. This range of windows was selected to capture the natural variability in the length scales of the observed bed forms. Variability in both quantities is roughly proportional to the mean with a coefficient of variation of 5% to 10% for Reynolds stress and 10% to 17% for transport rate.

[49] Figure 15a presents dimensionless transport rate $\tilde{q}_s^* = \tilde{q}_s / \sqrt{(R - 1)gD_m^3}$ versus dimensionless shear stress, or Shields Number $\tilde{\tau}_{u'w'}^* = \tilde{\tau}_{u'w'} / [(R - 1)\rho g D_m]$, where \tilde{q}_s and $\tilde{\tau}_{u'w'}$ are the total transport rate and instantaneous Reynolds stress averaged over the bed form time-scales, R is sediment specific gravity, g is gravitational acceleration, and D_m is the median grain size of the bed (7.7 mm). The trend closely matches that of the Meyer-Peter and Müller relation as modified by Wong and Parker [2006], suggesting that the bed form averaged instantaneous Reynolds stress represents the component of total stress driving sediment transport. To match the transport function to the observations, however, it is necessary to use a critical Shields Number $\tau_c^* = 0.03$, i.e., adapting the relation $q_s^* = 3.97(\tau_{u'w'}^* - 0.03)^{1.5}$ (see solid line in Figure 15a). This value of $\tau_c^* = 0.03$ is considerably smaller than the value of 0.047 found by Meyer-Peter and Müller to match the plane-bed transport of well-sorted gravels. A considerably smaller value, of order $u_c^* = 0.03$ has been found for the total transport of widely sorted sandy gravel mixtures [Wilcock, 1998], although general guidelines for the appropriate value of τ_c^* for the total transport rates of sandy gravel mixtures are not available.

[50] The observed transport rates can be compared to a specific transport prediction using the two-fraction transport model of Wilcock and Kenworthy [2002]. Figure 15b presents dimensionless transport rate $\tilde{q}_g^* = (p_g/f_g)\tilde{q}_g / \sqrt{(R - 1)gD_g^3}$ versus Shields Number $\tilde{\tau}_{u'w'}^* = \tilde{\tau}_{u'w'} / [(R - 1)\rho g D_m]$, where the subscript g indicates the gravel portion of the bed and transport, p_g is the fraction of gravel in transport, f_g is the fraction of gravel in the bed (76%), and D_g is the median grain size of gravel fraction in the bed (11.3 mm). A grain size of 4 mm separates the fine and coarse modes of the bed grain-size distribution and is used to define the boundary between ‘sand’ and ‘gravel’. Wilcock and Kenworthy [2002] found that two transport functions were needed to accommodate persistent differences between field and laboratory transport rates. An approximate form-drag correction was applied to all data used to develop the two-fraction functions and the difference between field and lab data was attributed to greater topographic

variability in the field. Because transport rates are a nonlinear function of shear stress, a bed with spatial variation in local shear stress will have larger transport rates than a plane bed with identical mean stress [Brownlie, 1981; Paola *et al.*, 1999]. Most flume data used in developing the Wilcock-Kenworthy transport relation had quasi-planar beds, whereas the field data had topographic variability at a range of scales. The flume data presented here closely match the field transport function, suggesting that the bed form averaged instantaneous Reynolds stress represents the form-drag corrected shear stress and that the spatial variability in stress produced by the bed forms produces greater transport rates.

8. Asymmetric Bed Elevation Increments and Interpretation of Multiscaling

[51] A number of multifractal models (e.g., random multiplicative cascade models) have been proposed in the literature to reproduce the multifractal nature of a signal or a function (e.g., rainfall, turbulence and other geophysical signals [Schertzer *et al.*, 1997]). In general, multiplicative cascades, having their origin in a phenomenological interpretation of the cascade of energy in turbulent eddies, are generated through a scale-invariant operator acting from the largest scale L down to the smallest scale l of the system. These models, by construction, produce symmetric pdfs at all scales. The important question that arises then is how one should interpret the statistical multiscaling reported herein within an energy cascade phenomenology in the presence of a significantly asymmetric pdf at all scales.

[52] We hypothesize that the answer to this question lies on a paradigmatic scale-coupling mechanism as that suggested by Warhaft [2002]. We suggest that multifractality and pdf asymmetry is the manifestation of a memory mechanism among scales, i.e., the small scale bed forms do not lose the information of their large scale counterparts, but instead there is an active coupling between large and small scales. In other words, the large scale geometric asymmetry of bed forms is carried down to a probabilistic asymmetry in the statistics of all smaller scale bed elevation increments (i.e., those in the stoss versus lee sides of the bed form), indicating thus a local anisotropy in the energy transfer. This hypothesis, which needs to be tested further, has the practical implication that the statistics of bed elevation increments obtained from plane bed topography are different compared to those obtained from a bed topography dominated by bed forms, even if the bed form non-stationarity effect has been filtered out. In other words, the coupling of scales renders a renormalization of the bed elevation series across discharges problematic.

9. Concluding Remarks

[53] The experiments reported in this study were conducted in a large experimental channel at the St. Anthony Falls Laboratory to understand the coupled dynamics of flow and bed forms above the sediment-water interface. Simultaneous high resolution measurements of velocity fluctuations, bed elevations, and sediment flux were made at the downstream end of the channel for a range of discharges. We analyzed the probabilistic structure of these quantities and especially quantified the behavior of their extreme

values (tails) and the asymmetry of these pdfs as function of discharge. We then employed multiscale analyses, both in Fourier and wavelet domains, to investigate the distribution of energy (variability) across scales and the scale-to-scale interactions, as well as, infer scales above which this scale dependence is lost implying the possibility, for example, of using time integrated quantities of instantaneous Reynolds stress as a predictor of sediment transport.

[54] The main results of this study can be stated as follows.

[55] 1. The probability density functions (pdfs) of bed elevation increments and instantaneous Reynolds stress reveal power law positive and negative tails. Bed elevation increments pdfs are well approximated by a truncated Pareto distribution and their extreme positive and negative tails (upper 95% quantile) were found to possess a fast-decaying power law behavior (almost exponential decay) suggesting that the truncation level of the truncated Pareto distribution can itself be approximated by an exponentially distributed random variable (a soft threshold suggestive of a tempered Pareto distribution).

[56] 2. A strong asymmetry in the pdfs of the bed elevation increments and instantaneous Reynolds stress was documented using both integrated metrics (such as the coefficient of skewness and the asymmetry index) as well as third order (localized) moment functions. It was shown that the positive tail asymmetry of bed elevation increments significantly increases with increasing discharge expressing the larger bed form height heterogeneity documented for larger discharges. Asymmetry in instantaneous Reynolds stress was interpreted by a quadrant analysis of longitudinal and vertical velocity fluctuations which also provided insight into the potential for particle entrainment (ejections and sweeps) contributing to sediment transport.

[57] 3. Spectral analysis of bed elevation time series revealed a power law behavior within scales of approximately 15 s and the maximum bed form timescale (i.e., the timescale associated with the largest passing bedforms). The spectral slope (of the order of 1.9 to 2.2) increased with increasing discharge implying a faster evolution of the multiscale bed structures at higher discharges, consistent with the faster decay of the scale-dependent celerity at higher discharges reported in Singh *et al.* [2011].

[58] 4. A higher order structure function analysis (motivated by the non-Gaussian pdfs) of bed elevation increments demonstrated the presence of multifractal scaling which was parameterized with two parameters: the roughness (expressing the global average of the strength of abrupt fluctuations) and the intermittency parameter (expressing the local variability of this roughness, i.e., the heterogeneity in the temporal arrangement of these abrupt fluctuations). Both the roughness parameter and the intermittency parameters were found to increase with increasing discharge.

[59] 5. The presence of intermittency (multifractality) in the bed elevation increments, in view of the asymmetric nature of the pdfs, was interpreted as the result of scale coupling, implying that the geometric asymmetry of the bed forms gets transferred down to a probabilistic asymmetry in the statistics of all smaller scale bed elevation increments. In view of a multifractal interpretation of energy transfer from large to small scales, such an asymmetry is an indication of a local anisotropy in the energy transfer.

[60] 6. The correlation between bed elevation and instantaneous Reynolds stress at multiple scales was found to increase with increasing scale suggesting that the bed structures can be inferred from flow structures sampled close to the bed, although the field application of this method would require a long time series of river flow velocities.

[61] 7. A predictive relationship between bed form averaged sediment transport rates and bed form averaged instantaneous Reynolds stress was proposed and shown to explain our observations within the quantified uncertainty.

[62] **Acknowledgments.** This research was supported by the National Center for Earth-surface Dynamics (NCED), a Science and Technology Center funded by NSF under agreement EAR-0120914 as well as by NSF grants EAR-0824084 and EAR-0835789. The support by a doctoral dissertation fellowship (A.S.) and the Ling Professorship (E.F.G.) at the University of Minnesota is gratefully acknowledged. The experiments performed for this study are the follow up of previous experiments (known as StreamLab06) conducted at the St. Anthony Falls Laboratory as part of an NCED program to examine physical-biological aspects of sediment transport (<http://www.nced.umn.edu>). The authors are thankful to Jeff Marr, Craig Hill and Sara Johnson for providing help in running the experiments. The authors are also thankful to Nate Bradley and two anonymous reviewers, as well as the Associate Editor, John Pitlick whose suggestions and constructive comments substantially improved our presentation and refined our interpretations. Computer resources were provided by the Minnesota Supercomputing Institute, Digital Technology Center at the University of Minnesota.

References

- Aban, I. B., M. M. Meerschaert, and A. K. Panorska (2006), Parameter estimation for the truncated Pareto distribution, *J. Am. Stat. Assoc.*, **101**(473), 270–277.
- Aberle, J., and V. Nikora (2006), Statistical properties of armored gravel bed surfaces, *Water Resour. Res.*, **42**, W11414, doi:10.1029/2005WR004674.
- Batchelor, G. K., and A. A. Townsend (1949), The nature of turbulent motion at high wave numbers, *Proc. R. Soc. London, Ser. A*, **199**, 238–255.
- Bennett, S. J., and J. L. Best (1995), Mean flow and turbulence structure over fixed, two-dimensional dunes: Implications for sediment transport and dune stability, *Sedimentology*, **42**, 491–513.
- Best, J. L. (1993), On the interactions between turbulent flow structure, sediment transport and bedform development: Some considerations from recent experimental research, in *Turbulence: Perspectives on Flow and Sediment Transport*, edited by N. J. Clifford, J. R. French, and J. Hardisty, pp. 61–92, Wiley, Chichester, U. K.
- Best, J. (2005), The fluid dynamics of river dunes: A review and some future research directions, *J. Geophys. Res.*, **110**, F04S02, doi:10.1029/2004JF000218.
- Boyer, C., A. G. Roy, and J. L. Best (2006), Dynamics of a river channel confluence with discordant beds: Flow turbulence, bed load sediment transport, and bed morphology, *J. Geophys. Res.*, **111**, F04007, doi:10.1029/2005JF000458.
- Brownlie, W. R. (1981), Prediction of flow depth and sediment discharge in open channels, *Rep. KH-R-43A*, W. M. Keck Lab. of Hydraul. and Water Resour., Calif. Inst. of Technol., Pasadena.
- Buffin-Bélanger, T. A., A. G. Roy, and A. D. Kirkbride (2000), On large-scale flow structures in a gravel-bed river, *Geomorphology*, **32**, 417–435.
- Castaing, B., Y. Gagne, and E. J. Hopfinger (1990), Velocity probability density-functions of high Reynolds-number turbulence, *Physica D*, **46**, 177–200.
- Clauset, A., C. R. Shalizi, and M. E. J. Newman (2009), Power law distributions in empirical data, *SIAM Rev.*, **51**(4), 661–703.
- Dinehart, R. L. (1992), Evolution of coarse gravel bedforms: Field measurements at flood stage, *Water Resour. Res.*, **28**(10), 2667–2689.
- Dinehart, R. L. (1999), Correlative velocity fluctuations over a gravel river bed, *Water Resour. Res.*, **35**(2), 569–582.
- Ganti, V., K. M. Straub, E. Foufoula-Georgiou, and C. Paola (2011), Space-time dynamics of depositional systems: Experimental evidence and theoretical modeling of heavy-tailed statistics, *J. Geophys. Res.*, **116**, F02011, doi:10.1029/2010JF001893.
- Hardy, R. J., J. L. Best, S. N. Lane, and P. E. Carbonneau (2009), Coherent flow structures in a depth-limited flow over a gravel surface: The role of near-bed turbulence and influence of Reynolds number, *J. Geophys. Res.*, **114**, F01003, doi:10.1029/2007JF000970.
- Hardy, R. J., J. L. Best, S. N. Lane, and P. E. Carbonneau (2010), Coherent flow structures in a depth-limited flow over a gravel surface: The influence of surface roughness, *J. Geophys. Res.*, **115**, F03006, doi:10.1029/2009JF001416.
- Jerolmack, D. J., and D. Mohrig (2005), A unified model for subaqueous bed form dynamics, *Water Resour. Res.*, **41**, W12421, doi:10.1029/2005WR004329.
- Kleinmans, M. G., A. W. E. Wilbers, A. De Swaaf, and J. H. Van Den Berg (2002), Sediment supply-limited bedforms in sand-gravel bed rivers, *J. Sediment. Res.*, **72**, 629–640, doi:10.1306/030702720629.
- Kolmogorov, A. N. (1941), The local structure of turbulence in incompressible viscous fluid for very large Reynolds number, *Dokl. Akad. Nauk. SSSR*, **30**, 299–303.
- Kumar, P., and E. Foufoula-Georgiou (1997), Wavelet analysis for geophysical applications, *Rev. Geophys.*, **35**(4), 385–412, doi:10.1029/97RG00427.
- Lamarre, H., and A. G. Roy (2005), Reach scale variability of turbulent flow characteristics in a gravel-bed river, *Geomorphology*, **60**, 95–113.
- Lu, S. S., and W. W. Willmarth (1973), Measurements of structure of Reynolds stress in a turbulent boundary layer, *J. Fluid Mech.*, **60**, 481–511.
- Maddux, T. B., J. M. Nelson, and S. R. McLean (2003), Turbulent flow over three-dimensional dunes: 1. Free surface and flow response, *J. Geophys. Res.*, **108**(F1), 6009, doi:10.1029/2003JF000017.
- Malecot, Y., C. Auriault, H. Kahalerras, Y. Gagne, O. Chanal, B. Chabaud, and B. Castaing (2000), A statistical estimator of turbulence intermittency in physical and numerical experiments, *Eur. Phys. J. B*, **16**, 549–561.
- Mallat, S. (1998), *A Wavelet Tour in Signal Processing*, Academic, San Diego, Calif.
- McLean, S. R., and J. D. Smith (1979), Turbulence measurements in the boundary layer over a sand wave field, *J. Geophys. Res.*, **84**(C12), 7791–7808.
- McLean, S. R., J. M. Nelson, S. R. Wolfe (1994), Turbulence structure over two-dimensional bed forms: Implications for sediment transport, *J. Geophys. Res.*, **99**, 12,729–12,747.
- Meerschaert, M. M., P. Roy, and Q. Shao (2012), Parameter estimation for tempered power law distributions, *Commun. Stat. Theory Methods*, **41**(10), 1839–1856.
- Nelson, J. M., S. R. McLean, and S. R. Wolfe (1993), Mean flow and turbulence fields over two-dimensional bedforms, *Water Resour. Res.*, **29**, 3935–3953.
- Nelson, J. M., R. L. Shreve, S. R. McLean, and T. G. Drake (1995), Role of near-bed turbulence structure in bed load transport and bed form mechanics, *Water Resour. Res.*, **31**(8), 2071–2086, doi:10.1029/95WR00976.
- Nelson, J. M., A. R. Burman, Y. Shimizu, S. R. McLean, R. L. Shreve, and M. W. Schmeeckle (2006), Computing flow and sediment transport over bedforms, *Proceedings of the 4th IAHR Symposium on River, Coastal and Estuarine Morphodynamics*, pp. 861–868, Taylor and Francis, Philadelphia, Pa.
- Nikora, V. I. (2008), Hydrodynamics of gravel-bed rivers: scale issues, in *Gravel-Bed Rivers VI: From Process Understanding to River Restoration*, edited by H. Habersack, H. Habersack, and M. Rinaldi, pp. 61–81, Elsevier, Boston, Mass.
- Nikora, V. I., and D. G. Goring (2000), Flow turbulence over fixed and weakly mobile gravel beds, *J. Hydraul. Eng.*, **126**(9), 679–690.
- Nikora, V. I., and J. Walsh (2004), Water-worked gravel surfaces: High-order structure functions at the particle scale, *Water Resour. Res.*, **40**, W12601, doi:10.1029/2004WR003346.
- Nikora, V. I., D. G. Goring, and B. J. F. Biggs (1998), On gravel-bed roughness characterization, *Water Resour. Res.*, **34**(3), 517–527.
- Paola, C., and L. Borgman (1991), Reconstructing random topography from preserved stratification, *Sedimentology*, **38**, 553–565, doi:10.1111/j.1365-3091.1991.tb01008.x.
- Paola, C., G. Parker, D. C. Mohrig, and K. X. Whipple (1999), The influence of transport fluctuations on spatially averaged topography on a sandy, braided fluvial plane, in *Numerical Experiments in Stratigraphy*, SEPM Spec. Publ., vol. 62, pp. 211–218, Soc. Sediment. Geol., Tulsa, Okla.
- Parsheh, M., F. Sotiropoulos, and F. Porté-Agel (2010), Estimation of power spectra of acoustic-doppler velocimetry data contaminated with intermittent spikes, *J. Hydraul. Eng.*, **136**, 368–378, doi:10.1061/(ASCE)HY.1943-7900.0000202.
- Roy, A. G., T. Buffin-Bélanger, H. Lamarre, and A. D. Kirkbride (2004), Size, shape and dynamics of large-scale turbulent flow structures in a gravel-bed river, *J. Fluid Mech.*, **500**, 1–27.
- Saupe, D. (1988), Algorithms for random fractals, in *The Science of Fractal Images*, edited by H.-O. Peitgen, and D. Saupe, pp. 71–136, Springer, New York.

- Schertzer, D., S. Lovejoy, F. Schmitt, Y. Chiguirinskaya, and D. Marsan (1997), Multifractal cascade dynamics and turbulent intermittency, *Fractals*, 5, 427–471.
- Schmeeckle, M. W., and J. M. Nelson (2003), Direct simulation of bedload transport using a local, dynamic boundary condition, *Sedimentology*, 50, 279–301.
- Shvidchenko, A. B., and G. Pender (2001), Macroturbulent structure of open-channel flow over gravel beds, *Water Resour. Res.*, 37(3), 709–719.
- Singh, A., K. Fienberg, D. J. Jerolmack, D. G. Marr, and E. Foufoula-Georgiou (2009a), Experimental evidence for statistical scaling and intermittency in sediment transport rates, *J. Geophys. Res.*, 114, F01025, doi:10.1029/2007JF000963.
- Singh, A., S. Lanzoni, and E. Foufoula-Georgiou (2009b), Nonlinearity and complexity in gravel-bed dynamics, *Stochastic Environ. Res. Risk Assess.*, 23(7), 967–975, doi:10.1007/S00477-008-0269-8.
- Singh, A., F. Porté-Agel, and E. Foufoula-Georgiou (2010), On the influence of gravel bed dynamics on velocity power spectra, *Water Resour. Res.*, 46, W04509, doi:10.1029/2009WR008190.
- Singh, A., S. Lanzoni, P. R. Wilcock and E. Foufoula-Georgiou (2011), Multi-scale statistical characterization of migrating bedforms in gravel and sand bed rivers, *Water Resour. Res.*, 47, W12526, doi:10.1029/2010WR010122.
- Sumer, B. M., L. H. C. Chua, N.-S. Cheng, and J. Fredsøe (2003), Influence of turbulence on bed load sediment transport, *J. Hydraul. Eng.*, 129, 585–596.
- van der Mark, C. F., A. Blom, and S. J. M. H. Hulscher (2008), Quantification of variability in bedform geometry, *J. Geophys. Res.*, 113, F03020, doi:10.1029/2007JF000940.
- Venditti, J. G. (2007), Turbulent flow and drag over fixed two- and three-dimensional dunes, *J. Geophys. Res.*, 112, F04008, doi:10.1029/2006JF000650.
- Venugopal V., F. Porté-Agel, E. Foufoula-Georgiou, and M. Carper (2003), Multiscale interactions between surface shear stress and velocity in turbulent boundary layers, *J. Geophys. Res.*, 108(D19), 4613, doi:10.1029/2002JD003025.
- Venugopal, V., S. G. Roux, E. Foufoula-Georgiou, and A. Arneodo (2006), Revisiting multifractality of high-resolution temporal rainfall using a wavelet-based formalism, *Water Resour. Res.*, 42, W06D14, doi:10.1029/2005WR004489.
- Warhaft, Z. (2002), Turbulence in nature and in the laboratory, *Proc. Natl. Acad. Sci. USA*, 99, 2481–2486.
- Wiberg, P. L., and J. M. Nelson (1992), Unidirectional flow over asymmetric and symmetric ripples, *J. Geophys. Res.*, 97(C8), 12,745–12,761, doi:10.1029/92JC01228.
- Wilcock, P. R. (1998), Two-fraction model of initial sediment motion in gravel-bed rivers, *Science*, 280, 410–412.
- Wilcock, P. R., and S. T. Kenworthy (2002), A two-fraction model for the transport of sand/gravel mixtures, *Water Resour. Res.*, 38(10), 1194, doi:10.1029/2001WR000684.
- Wilcock, P. R., C. H. Orr, and J. D. G. Marr (2008), The need for full-scale experiments in river science, *Eos Trans. AGU*, 89(1), 6, doi:10.1029/2008EO010003.
- Wong, M., and G. Parker (2006), Reanalysis and correction of bed-load relation of Meyer-Peter and Müller using their own database, *J. Hydraul. Eng.*, 132, 1159–1168.